

# Near-field development of large-scale vortical structures in a controlled confined coaxial jet

Akihiko Mitsuishi, Koji Fukagata, Nobuhide Kasagi

June 23, 2006

## Abstract

We carry out direct numerical simulation (DNS) of scalar transport and mixing in a coaxial round jet issued into a small model combustor. The Reynolds number based on the diameter and bulk mean velocity of the outer annular jet is 1320. The outer-to-inner bulk mean velocity ratio is fixed at 6.4. Analysis is made on the detailed mechanism of scalar transport modulated by an active control of the near-field large-scale vortical structure. The main interest lies in dynamics of the vortical structure created by the present active control method, growth of streamwise vorticity, and the associated scalar transport process downstream of the nozzle exit. The mixing enhancement is found to be due to three-dimensional breakdown of the primary vortex rings in the inner shear layer. This breakdown process is caused by the streamwise vortical structure. Budget analysis reveals different dynamic processes taking place in the evolution of streamwise structure in the inner and outer shear layers. The process in the outer shear layer is essentially similar to that in plane mixing layers, while the structure in the inner shear layer is convected toward the central axis before stretched axially by the inner vortex rings.

## 1 Introduction

Coaxial jet flows are widely used in industrial applications, such as gas turbine combustors and chemical reactors, where mixing of different fluids takes place. There are many devices to passively control the flow field inside such equipment (e.g. swirlers and non-circular nozzles) in order to improve the performance at its design point. However, for small-scale combustors, such as those used in distributed generation systems, the power output often shifts off the design point. In such cases, the passive control methods are no longer effective and we need to rely on some active control methods.

Previous experimental studies have demonstrated that the performance of a coaxial jet combustor can be controlled by manipulation of the near-field large-scale vortical structure, which leads to modulation of reactant transport. Suzuki *et al.* [1] developed a special nozzle called ‘intelligent nozzle’, which has eighteen miniature electromagnetic flap actuators mounted on the periphery of

the outer nozzle, and can manipulate the near-field vortical structure in the jet. Kurimoto *et al.* [2] extended this technique to a coaxial jet combustion, as shown in figure 1, and successfully stabilized the unsteady motion of the base of a lifted methane-air flame even under a blow-off condition. Kurimoto [3] also reduced the entire heat release fluctuation of bluff-body stabilized flames inside a small model combustor. Based on the experimental results, he suggested that the controllability of the fuel concentration distribution upstream of the flame front should be an important factor for the performance of the model combustor. Recently, Angele *et al.* [4] experimentally investigated the evolution of three-dimensional structure in a free coaxial jet controlled by the intelligent nozzle [2]. By using stereoscopic particle image velocimetry (PIV), they observed strong streamwise vortices in the inner part of the jet, and conjectured that those vortices might play important roles for the mixing enhancement. Despite these experimental efforts, however, detailed mechanism of this control still remains unclear.

Direct numerical (DNS) and large-eddy (LES) simulations have been reported for various type of jet flows, e.g. DNS of a free round jet by Danaila *et al.* [5] and Boersma *et al.* [6], DNS of a free coaxial jet by da Silva *et al.* [7], and LES of a confined coaxial jet at practically high Reynolds numbers by Akselvoll and Moin [8]. These studies revealed detailed dynamics of the vortical structure in uncontrolled jets, and demonstrated that DNS and LES serve as powerful analysis tools.

The objective of the present study is to investigate by means of DNS the detailed dynamics of large-scale vortical structure in a coaxial jet controlled by the intelligent nozzle [2]. The present control aims at better mixing of scalar, which corresponds to mixing of fuel and air, under a relatively low Reynolds number condition. Therefore, we mainly focus upon the vortical structure associated with the initial scalar transport right downstream of the nozzle, which largely affects the mixing behaviour in the further downstream region. In section 2, we present the numerical method used and model the control input produced by the intelligent nozzle. The overall effects of the control amplitude and frequency are surveyed in section 3. In section 4, scalar transport by primary vortex rings is briefly described in the case where the best mixing is achieved in section 3. Subsequently, in section 5, the detailed mechanism of large-scale structure associated with the initial scalar transport observed in the present DNS is discussed. Finally, in section 6, conclusions are drawn together with the summary of mechanisms revealed by the present DNS.

## 2 Numerical method

Figure 2 shows the computational model used in this study. Coaxial central and annular jets are issued into a cylindrical space. Diameters (radii) of the inner and outer nozzles and the cylinder are denoted as  $D_i$  ( $R_i$ ),  $D_o$  ( $R_o$ ), and  $D_w$  ( $R_w$ ), respectively. The outer-to-inner diameter ratio,  $D_o/D_i$ , is two and the expansion ratio,  $D_w/D_o$ , is also two.

The governing equations are the incompressible continuity and Navier-Stokes equations, and the transport equation of a passive scalar:

$$\nabla \cdot \mathbf{u} = 0, \quad (1)$$

$$\frac{\partial \mathbf{u}}{\partial t} = -\nabla \cdot (\mathbf{u}\mathbf{u}) - \nabla p + \frac{1}{\text{Re}} \nabla^2 \mathbf{u}, \quad (2)$$

$$\frac{\partial c}{\partial t} = -\nabla \cdot (c\mathbf{u}) + \frac{1}{\text{Re Sc}} \nabla^2 c, \quad (3)$$

where  $\mathbf{u}$ ,  $p$ ,  $t$ , and  $c$  denote the dimensionless velocity vector, pressure, time, and passive scalar concentration, respectively. All the flow variables are normalized hereafter by the bulk mean velocity of the annular jet,  $U_{m,o}$ , and the outer nozzle diameter,  $D_o$ . Focusing on a small methane/air combustor, of which power output is 0.5–1 kW, the Reynolds number  $\text{Re}$  based on  $U_{m,o}$  and  $D_o$  is set at 1320. The outer-to-inner bulk mean velocity ratio,  $\beta = U_{m,o}/U_{m,i}$ , is 6.4. Namely, the outer-to-inner momentum flux ratio is 41, which corresponds to the equivalence ratio of 0.72 if we assume the complete mixing of methane from the central nozzle and air from the annulus. The Schmidt number  $\text{Sc}$  of the passive scalar is assumed to be unity, which nearly corresponds to the diffusion of methane into air at the standard temperature and pressure.

Fully developed laminar velocity profiles are assumed at the inlet of the coaxial jet. White noise with its amplitude of one percent of  $U_{m,o}$  is superposed on the streamwise component of the jet inlet velocity. The local scalar concentration  $c$  is represented by the mixture fraction of the central jet fluid, which takes the values of  $c = 1$  and  $c = 0$  for the inner and outer nozzles, respectively. The convective boundary condition [8] is employed for both velocity and scalar concentration at the outlet of the computational domain. The global mass conservation is enforced by multiplying a uniform correction factor  $(1 + \alpha)$  to the outlet velocity profile at every computational time step. The typical magnitude of  $\alpha$  is  $10^{-8}$ . On the lateral and bottom walls, no-slip boundary condition is imposed for the velocity and the scalar flux is fixed at zero.

A schematic diagram of the control effect is shown in figure 3. As shown in the figure, the actuation by the intelligent nozzle is modelled as a spatiotemporal change of the inlet velocity profile. We focus on the axisymmetric mode of the control, i.e. inphase motion of all the actuators. The outer nozzle radius,  $R_a$ , is contracted sinusoidally as

$$R_a(t) = R_o - \varepsilon [1 - \cos(2\pi \text{St}_a t)], \quad (4)$$

where the Strouhal number,  $\text{St}_a$ , and  $\varepsilon$  denote the normalized frequency and amplitude of flapping motion, respectively. Since the volumetric flow rate is kept constant, the axial and radial velocities at the annular jet exit are modelled as

$$u_z(r, \theta, 0, t) = U_0(r; R_a(t), R_i) \left/ \frac{R_a(t)^2 - R_i^2}{R_o^2 - R_i^2} \right., \quad (5)$$

$$u_r(r, \theta, 0, t) = \frac{dR_a(t)}{dt} = -2\pi \text{St}_a \varepsilon \sin(2\pi \text{St}_a t), \quad (6)$$

where  $U_0(r; a, b)$  denotes the analytical solution of fully developed laminar flow in an annular pipe, of which outer and inner radii are  $a$  and  $b$ . The inlet velocity profile of the inner jet is kept parabolic during the control. Figure 4 shows the radial profiles of the inflow streamwise velocity at different control phase angles. By periodically contracting the outer radius of the annular nozzle, the maximum streamwise velocity of the annular jet increases by more than 10%.

The governing equations (1)-(3) are discretized on the cylindrical coordinate system by using the energy-conservative second-order central difference scheme [9], except that the total variation diminishing (TVD) scheme [10] is used for the advection term of equation (3). The computational domain consists of  $64 \times 64 \times 256$  grids along the radial ( $r$ ), azimuthal ( $\theta$ ), and axial ( $z$ ) directions, respectively. As shown in figure 5, the grid is unequally spaced in the radial direction, so that it is clustered near the lateral wall and around the two free shear layers (i.e. near the inner and outer nozzle edges). The grid is uniform in the axial and azimuthal directions. The axial domain length,  $L_z$ , is set to  $8D_o$ , so that most of the important flow structure of a confined annular jet [11] can be captured.

The low storage third-order Runge-Kutta/Crank-Nicolson scheme [12] is used for the time integration, and the delta-form fractional step method [13] is employed for the pressure velocity coupling. The dimensionless time step,  $\Delta t$ , is 0.002 for all simulation cases. Time marching is started with a completely stationary field with zero-concentration fluid. The numerical method used in the present study is basically the same as that of the previous DNS of pipe flow [9]. The pressure-Poisson equation with the inflow and outflow boundary conditions is solved by using FFT with the aid of reflection operation [14], as shown in figure 6. This algorithm is equivalent to apply a discrete cosine transform to an interpolated pressure,  $\Phi_{k+1/2} = (\phi_k + \phi_{k+1})/2$ .

Validation and verification of the present simulation method are reported in detail in [15]. For example, as shown in figure 7, the mean and root-mean-square (rms) fluctuations of the axial velocity along the central axis of an uncontrolled confined annular jet computed by the present simulation code are in good agreement with the experimental data of [11]. The number of grids as well as the size of computational domain used is found sufficient for obtaining unique profiles of statistical quantities [15]. The influence of the convective outflow condition is investigated by simulations of a confined annular flow with various domain lengths. Figure 8 shows the rms fluctuations of the streamwise velocity at  $D_o/D_i = 2.09$ ,  $D_w/D_o = 1.99$ , and  $\text{Re} = 1270$  (the same conditions as [11]). With  $L_z/D_o = 8$ , the position and intensity of the peak are well reproduced and the near field statistics are converged to a unique profile.

In the following analysis, we often use phase-averaged statistics. According to Hussain and Zaman [16], an instantaneous value ( $\tilde{g}$ ) of any quantity ( $g$ ) is decomposed as:

$$\tilde{g}(r, \theta, z, t) = \langle g \rangle_\psi(r, z) + g'(r, \theta, z, t). \quad (7)$$

Here,  $\langle \bullet \rangle_\psi$  denotes the phase-average, which is the summation of the time mean and the periodic component at the control phase-angle of  $\psi$ , i.e.

$$\langle g \rangle_\psi(r, z) \equiv \lim_{N \rightarrow \infty} \frac{1}{2\pi N} \sum_{n=1}^N \left[ \int_0^{2\pi} \tilde{g}(r, \theta, z, t_{\psi n}) d\theta \right] \quad (8)$$

where  $t_{\psi n} = \frac{1}{2\pi \text{St}_a} (\psi + 2n\pi)$ , and  $g'$  is the residual random component. The phase-averaged rms fluctuations of  $\tilde{g}$  is then defined as

$$\begin{aligned} \langle g \rangle_{\psi, \text{rms}}(r, z) &\equiv \sqrt{\langle g'^2 \rangle_\psi(r, z)} \\ &= \sqrt{\lim_{N \rightarrow \infty} \frac{1}{2\pi N} \sum_{n=1}^N \left[ \int_0^{2\pi} g'^2(r, \theta, z, t_{\psi n}) d\theta \right]}. \end{aligned} \quad (9)$$

### 3 Overview of the control effects

Instantaneous vortical structure and concentration of the scalar ejected from the central nozzle are visualized in figure 9. The vortical structure is identified by the second invariant of the deformation rate tensor. Four uncontrolled cases at different values of  $\beta$  (velocity ratio) are shown. For the controlled case, only one case of  $\beta$  is shown because the flow pattern is found not significantly dependent on  $\beta$ . The control amplitude and frequency are  $\varepsilon = 0.0125$  and  $\text{St}_a = 1$ , at which the best mixing is achieved in the experiment [17]. Without control, a low-Re coaxial jet can generate a variety of flow patterns depending on  $\beta$ , as shown in figures 9(a)-(d). An initially laminar flow undergoes transition to turbulence in a high  $\beta$  case. Roll-up vortices from the inner shear layer can clearly be seen due to the high shear between the outer and inner jets (figure 9(a)). For the cases of small  $\beta$ , another flow pattern appears, where turbulent motion is suppressed and mixing is very poor (figures 9(b) and (d)). At a certain  $\beta$  of  $8 < \beta < 10$ , a special flow pattern appears (see, figure 9(c)); the diverging jet forms a large recirculation bubble at the center of the domain. Similar flow patterns have been experimentally observed in a confined annular jet at low Reynolds numbers [11]. With control, however, such diversity of flow patterns vanishes. Large-scale vortex rings are generated in the near field of the nozzle and they promptly break down intensifying the scalar mixing (see, figure 9(e)).

The mean velocity fields are shown in figure 10 for two different cases of  $\varepsilon = 0.001$  and  $\varepsilon = 0.01$  at  $\beta = 6.4$  in order to investigate the effects of control

amplitude. The control frequency is kept at  $St_a = 1$ . Note that the radial positions of  $r/D_o = 0.25$  and  $0.5$  correspond to the inner and outer shear layers of the intelligent nozzle, respectively. The velocity vectors are parallel to  $z$ -axis at  $z/D_o = 4$  in both cases. The upstream flow structure largely depends on  $\varepsilon$ . With small  $\varepsilon$ , the annular flow reattaches to the lateral wall in a shorter distance than the large  $\varepsilon$  case. The annular flow detaches just downstream of this reattachment point and it forms a recirculation zone around the central axis.

The phase-averaged azimuthal vorticity profiles for  $St_a = 0.5, 1$  and  $1.5$  are shown in figure 11. As is clear from comparison between the cases of  $St_a = 0.5$  and  $1$ , the interval of two successive vortex rings is lengthened with decreasing  $St_a$ . Moreover, the magnitude of vorticity is reduced for smaller  $St_a$ , because the radial velocity at the inlet, which determines the initial roll-up vorticity, is proportional to  $St_a$  in the present study as defined in equation (6). Namely, intermittent generation of weak vortices causes poorer mixing between the jet and ambient quiescent fluid at smaller  $St_a$ . On the other hand, comparison between the cases of  $St_a = 1$  and  $1.5$  indicates that the path of vortex rings is straightened with increasing  $St_a$ . This suggests that vortex rings are stabilized at higher  $St_a$ . As will be discussed in section 5.4, the stretching motion along the central axis is essential for the development of streamwise vortical structure which destabilize the vortex rings. At higher  $St_a$ , this stretching motion is weakened as the vortex rings come too close to each other. The development of streamwise vortices is suppressed accordingly. Thus, mixing becomes poor also at higher  $St_a$ . Due to these two mechanisms, there exists an optimum value of  $St_a$  to obtain the best mixing.

Figure 12 summarizes the effect of the control parameters, i.e. amplitude and frequency. Here, based on the observation above, we choose the reattachment length,  $L_R$ , as a representative measure of the control effect. The reattachment length is defined as a streamwise distance between the nozzle exit and the reattachment point on the lateral wall, where  $\partial u_z / \partial r$  is zero on average. As shown in figure 12(a),  $L_R$  is much shorter for  $\varepsilon \leq 0.0025$  than for  $\varepsilon \geq 0.003$  at  $St_a = 1$ . The sudden jump of  $L_R$  between  $\varepsilon = 0.0025$  and  $0.003$  indicates discontinuous change of the flow structure observed in figure 10. Beyond  $\varepsilon = 0.003$ ,  $L_R$  decreases monotonically as the control amplitude increases due to the rapid growth of the outer shear layer. On the other hand, as shown in figure 12(b),  $L_R$  smoothly varies with  $St_a$  with keeping  $\varepsilon$  at a sufficiently large value of  $0.0125$ . In the figure,  $L_R$  takes its minimum value when  $St_a$  is around  $0.7$ . The existence of the minimum  $L_R$  suggests that the two mechanisms discussed in figure 11 restrict the development of the shear layers.

In order to study the effect of  $St_a$  on the scalar mixing, radial distributions of the phase-averaged scalar concentration at different axial positions are shown in figure 13 for  $St_a = 0.5, 1$  and  $1.5$ . Among the three  $St_a$  tested, the case of  $St_a = 1$  achieves the best mixing at  $z/D_o = 2$ . In this case, the concentration has less fluctuations among the five control phase-angles than that of  $St_a = 0.5$ , and the scalar permeate the radial extent more than that of  $St_a = 1.5$ . Also, in this case, the concentration starts decreasing at the nearest position from the

inlet (see, the profiles at  $z/D_o = 0.5$  of three figures). In the case of  $St_a = 0.5$ , the scalar has large fluctuations even at  $z/D_o = 2$  due to the intermittent generation of the vortex rings as has been observed in figure 11(a). In the case of  $St_a = 1.5$ , the upstream mixing region is narrower in radial direction than that of  $St_a = 1$ , and thus the fluid with high concentration remains near the central axis even at  $z/D_o = 2$ .

The effect of control frequency on the mean scalar concentration along the central axis is examined. Comparison between the previous experimental results of a controlled free coaxial jet [3] is shown in figure 14(a). Despite the difference in the Reynolds number and flow configuration, the present computational results are in fair agreement with the experimental data. The agreement is especially good for  $St_a = 1$  and 1.3, where good mixing is achieved. Figure 14(b) shows the effect of control frequency in the present study. Regardless of the frequency selected, mixing is better than the uncontrolled case. The cases studied are classified into three regimes: (i)  $St_a < 0.7$ ; (ii)  $0.7 < St_a < 1.1$ ; (iii)  $1.1 < St_a$ . In regimes (i) and (iii), mixing is relatively weak as has been shown in figure 13. On the other hand, the regime of (ii) achieves the earliest attenuation of the concentration along the central axis among all the cases examined, which supports the observation in figure 13. In this regime, the profiles are relatively independent of  $St_a$ , which implies that the mixing enhancement is achieved by a certain mechanism which is not strongly affected by  $St_a$ . This mixing enhancement mechanism is studied in later sections.

## 4 Scalar transport by primary vortex rings

Detailed mechanism of the scalar transport is studied by examining the phase-averaged statistics. Here we focus on the case of  $\varepsilon = 0.0125$  and  $St_a = 0.9$ , where strong mixing along the central axis was achieved.

The distribution of phase-averaged azimuthal vorticity,  $\langle \omega_\theta \rangle_\psi$ , is shown in figure 15 for five different control phases, i.e.  $\psi = 2\pi M/5$  with  $M$  being 0, 1, 2, 3 and 4. The figure indicates how the present control generates the large-scale vortical structure in the near-field. We can clearly observe that a pair of counter-rotating vortex rings are discharged at the frequency of control. This roll-up of the inner and outer shear layers is the primary effect of the present control.

Effects of the discharged vortex rings on the phase-averaged velocity,  $\langle u_z \rangle_\psi$ , and scalar,  $\langle c \rangle_\psi$ , fields are shown in figures 16 and 17, respectively. There are alternatively high- and low-speed regions along the streamwise direction both in inner and outer jets (see, figure 16). Especially, a backflow region is found near the central axis, which is due to the inner roll-up vortices with negative azimuthal vorticity. Due to this backflow, the central jet is stagnated around  $z/D_o = 0.5$ . The scalar concentration along the central axis abruptly drops upstream of the stagnation region (see, figure 17). Most of the scalar is then wound up by the inner vortex ring, not by the outer one, and convected downstream.

## 5 Production processes of streamwise vorticity

As shown above, dynamics and downstream evolution of the inner vortex rings are important for the mixing enhancement. Therefore, in this section, the dynamics of large-scale three-dimensional coherent structure related to the primary vortex rings are investigated in detail. Special attention is paid to the evolution of streamwise vortices.

### 5.1 Streamwise vortical structure around the primary vortex rings

Distributions of the phase-averaged rms fluctuations of the radial,  $\langle \omega_r \rangle_{\psi, \text{rms}}$ , and axial,  $\langle \omega_z \rangle_{\psi, \text{rms}}$ , vorticity are shown in figure 18 for the control phase-angle of  $\psi = 1.6\pi$ . These quantities indicate how the initially two-dimensional large-scale vortex rings generate three-dimensional structure. A remarkable observation is that  $\langle \omega_z \rangle_{\psi, \text{rms}}$  is highly localized, e.g. at  $(r/D_o, z/D_o) = (0.1, 0.8)$ ,  $(0.6, 0.6)$  and  $(0.6, 1.3)$ , while the peaks of  $\langle \omega_r \rangle_{\psi, \text{rms}}$  are relatively wide. This implies that the streamwise vortical structure arises locally by a certain mechanism related to the present control, while the radial vorticity appears to be due to the random motion of the broken vortices downstream.

The phase-averaged azimuthal vorticity,  $\langle \omega_\theta \rangle_\psi$ , and the phase-averaged rms fluctuations of the axial vorticity component,  $\langle \omega_z \rangle_{\psi, \text{rms}}$ , are shown together in figure 19. In the figure, local maxima of  $\langle \omega_z \rangle_{\psi, \text{rms}}$  that come from the inner shear layer are labelled as (A) and are numbered in order of their development as (A1-17), and those of the outer shear layer are similarly labelled as (B1-16). The peaks of (A7-11) exist between the inner vortex rings and are stretched due to the induced velocity field. This mechanism is similar to that of ‘rib’ vortices (see, e.g. [18–22]). On the other hand, the peaks of (B7-16) are found near the outer vortex rings. Interpretation of these outer streamwise vorticity, i.e. (B7-16), is twofold: there are coherent streamwise vortices crowded near the rings, or distortion of the rings is counted as the streamwise vorticity fluctuation (or both). An instantaneous close-up picture near this region, which is shown in figure 20, indicates that the streamwise vorticity corresponding to (A) consists of several streamwise vortices ((i) in the figure), while that to (B) seem to be accompanied by the distortion of the outer vortex rings ((ii) in the figure).

### 5.2 Transport equation of fluctuation intensity of streamwise vorticity

The origin and the growth of the streamwise vortical structure are investigated by the phase-averaged transport equation of streamwise vorticity fluctuation, which reads

$$\begin{aligned} \frac{\partial}{\partial t} \left\langle \frac{1}{2} \omega_z^2 \right\rangle &= CV_{r\psi} + CV_{z\psi} + TD_\psi + VD_\psi + DS_\psi \\ &+ PR_r^{\text{mvg}}_\psi + PR_z^{\text{mvg}}_\psi + PR_\theta^{\text{mix}}_\psi + PR^{\text{fv}}_\psi. \end{aligned} \quad (10)$$

The terms appearing on the right-hand side of equation (10) and their physical meanings [23] are summarized in table 1. Note,  $\langle u_\theta \rangle_\psi$ ,  $\langle \omega_r \rangle_\psi$ ,  $\langle \omega_z \rangle_\psi$ , and  $\partial \langle \bullet \rangle_\psi / r \partial \theta$  are zero in the problem considered here.

Among these terms, we focus on the production due to the phase-averaged velocity gradient in radial ( $PR_r^{\text{mvg}}_\psi$ ) and axial ( $PR_z^{\text{mvg}}_\psi$ ) directions, and the azimuthal mixed production ( $PR_\theta^{\text{mix}}_\psi$ ). Generally speaking, the production by the fluctuating velocity gradient,  $PR^{\text{fv}}_\psi$ , is one of the dominant terms in uncontrolled jets [23]. In the present controlled coaxial jet, however, its amplitude is found much smaller than the above-mentioned three terms.

Figures 21-23 show the distributions of  $PR_r^{\text{mvg}}_\psi$ ,  $PR_z^{\text{mvg}}_\psi$ , and  $PR_\theta^{\text{mix}}_\psi$  for the case of  $St_a = 1$ . There are some similarities and dissimilarities between the production processes of the streamwise vorticity fluctuation near the central axis and along the outer shear layer, which are labelled in figure 19 as (A) and (B). Details are discussed in the following sections.

### 5.3 First stage: amplification by initial velocity gradient

For both (A) and (B), the seeds of axial vorticity, of which origin will be discussed later in section 5.5, are at first intensified by  $PR_r^{\text{mvg}}_\psi$ . In figure 21, local maxima of  $PR_r^{\text{mvg}}_\psi$  are clearly seen on the ridges of  $\langle \omega_z \rangle_{\psi, \text{rms}}$  ((A7-9) and (B4-8) in the figure). This is due to the initial velocity gradient,  $\partial \langle u_z \rangle_\psi / \partial r$ . This early stage of production takes place just upstream of the first roll-up vortices induced by the control; the two-dimensional primary vortex rings stretch the upstream seeds of the three-dimensional structure before the next primary vortices roll up. Note that so-called braid region is not formed yet because the next primary vortex has not appeared. With the formation of the next primary vortices, the braid region appears. The streamwise structure is further stretched in a similar manner as in an ordinary mixing layer.

### 5.4 Second stage: differentiation of inner and outer structure

The structures evolved near the nozzles, (A) and (B), start to develop differently. For (A), the peak is mainly produced by  $PR_z^{\text{mvg}}_\psi$ , whereas  $PR_r^{\text{mvg}}_\psi$  is weakened and its effect is restricted to the downstream tail of the peaks of (A10-17) in figure 22. For (B), on the other hand,  $PR_r^{\text{mvg}}_\psi$  becomes even stronger than in the first stage, and at the same time, negative production of  $PR_\theta^{\text{mix}}_\psi$  appears which is found in figure 23 ((B9-16) in the figure).

There are two major reasons why  $PR_z^{\text{mvg}}_\psi$  replaces  $PR_r^{\text{mvg}}_\psi$  for the production process of (A) in the second stage. First,  $\partial \langle u_z \rangle_\psi / \partial r$  contained in

$PR_r^{\text{mvg}}_\psi$  approaches zero near the central axis due to the axisymmetry. Second,  $\partial \langle u_z \rangle_\psi / \partial z$  (which determines the sign of  $PR_z^{\text{mvg}}_\psi$ ) switches its sign along the central axis due to the intrusion by ‘arms’ of the inner roll-up vortices (see, distributions of streamwise velocity along  $r/D_o = 0$  in figure 16).

However, for the following two reasons, this  $PR_z^{\text{mvg}}_\psi$  is regarded as a mechanism to sustain, not to generate, the streamwise vorticity fluctuation. First, the region of  $PR_z^{\text{mvg}}_\psi > 0$  is always crowned by a cap of negative production of  $PR_z^{\text{mvg}}_\psi$  just upstream. The periodic intrusion by the inner vortex rings along the central axis also makes negative velocity gradient which acts as negative production. Second,  $PR_z^{\text{mvg}}_\psi$  needs a source of streamwise vorticity, which has been grown in the first stage and then convected radially by the subsequent inner vortex rings.

Unlike (A),  $\partial \langle u_z \rangle_\psi / \partial r$  of (B) does not decay downstream (see, figure 16). At the same time, however, negative production by the azimuthal mixed production,  $PR_\theta^{\text{mix}}_\psi$ , rapidly grows as shown in figure 23. The negative value of  $PR_\theta^{\text{mix}}_\psi$  appears because the distorted primary vortex is clung by ‘rib’ vortices that rotate in the opposite direction at the point where the primary vortex inclines itself in the azimuthal direction, and its axial vorticity is weakened by their motion (see, e.g. figure 14(b) of [24]). A slightly weak positive peak of  $PR_\theta^{\text{mix}}_\psi$  appearing downstream of the negative one is caused simply by elongation of the relevant rib vortices. When the rib vortices are elongated, they occasionally occupy the regions of opposite sign of  $\langle \omega_\theta \rangle_\psi$ , and then the sign of  $PR_\theta^{\text{mix}}_\psi$  turns to be positive. It is worth noting that the negative value of  $PR_\theta^{\text{mix}}_\psi$  cannot be explained only by the distortion of vortex rings. With distortion of the vortex rings only,  $PR_\theta^{\text{mix}}_\psi$  would have positive values regardless of the sign of  $\langle \omega_\theta \rangle_\psi$  because the primary vortices are aligned with the direction of the azimuthal gradient of the axial velocity.

The growth of the streamwise structure in the second stage is summarized as follows. As the inner streamwise structure is convected away from the inner shear layer, the leading mechanism of their development shifts to the axial stretching near the central axis. The axial stretching acting especially on the peak of the streamwise vorticity is caused by the periodically discharged inner vortex rings. On the other hand, the outer streamwise structure is formed by the rib vortices (as evidenced by the negative azimuthal mixed production). Similarly to the first stage, they are further intensified by the velocity gradient in the outer shear layer.

## 5.5 Before the first stage: generation of the streamwise structure

Finally, we explore the generation mechanisms at the very beginning of the development ((A1-6) and (B1-3) in figure 19), i.e. the step before the first stage described in section 5.3. We focus on the inner shear layer, where the mixing of scalar is mostly enhanced. Figure 24 shows the close-up pictures of the above-mentioned three production terms near the nozzle exit. The control phase-angle

is  $1.6\pi$  and  $0\pi (= 2\pi)$ . The gap of the colour contour levels is finer than that used in figures 21-23 to make it easy to identify the small amount of the initial production.

According to the figure, the initiation of the streamwise vorticity is governed by the balance of the radial stretching,  $PR_r^{\text{mvg}}_\psi$ , and the azimuthal mixed production,  $PR_\theta^{\text{mix}}_\psi$ . A claw-like structure is clearly observed in  $0 < z/D_o < 0.2$  for both  $PR_r^{\text{mvg}}_\psi$  and  $PR_\theta^{\text{mix}}_\psi$  with opposite sign. In fact,  $PR_r^{\text{mvg}}_\psi$  and  $PR_\theta^{\text{mix}}_\psi$  are negatively correlated. By their definition,  $PR_r^{\text{mvg}}_\psi$  and  $PR_\theta^{\text{mix}}_\psi$  are decomposed as

$$PR_r^{\text{mvg}}_\psi = \langle \omega'_z \omega'_r \rangle_\psi \frac{\partial \langle u_z \rangle_\psi}{\partial r} = \left\langle \omega'_z \left( \frac{\partial u'_z}{r \partial \theta} - \frac{\partial u'_\theta}{\partial z} \right) \right\rangle_\psi \frac{\partial \langle u_z \rangle_\psi}{\partial r}, \quad (11)$$

$$PR_\theta^{\text{mix}}_\psi = \langle \omega_\theta \rangle_\psi \left\langle \omega'_z \frac{\partial u'_z}{r \partial \theta} \right\rangle_\psi = \left( \frac{\partial \langle u_r \rangle_\psi}{\partial z} - \frac{\partial \langle u_z \rangle_\psi}{\partial r} \right) \left\langle \omega'_z \frac{\partial u'_z}{r \partial \theta} \right\rangle_\psi. \quad (12)$$

If the flow structure would not change in the streamwise direction (i.e.  $\partial u'_\theta / \partial z$  and  $\partial \langle u_r \rangle_\psi / \partial z$  are zero), then  $PR_r^{\text{mvg}}_\psi$  and  $PR_\theta^{\text{mix}}_\psi$  would become identical with opposite sign. Namely, the residual terms, i.e.  $\partial u'_\theta / \partial z$  and  $\partial \langle u_r \rangle_\psi / \partial z$ , break the equilibrium in the production mechanism at this stage. Table 2 shows the time evolution of  $\partial \langle u_r \rangle_\psi / \partial z$  at the inlet inner shear layer ( $r/D_o = 0.25$ ,  $z/D_o = 0$ ), which is a quantity controlled by the present nozzle. In the table, the other term appearing in equation (12),  $\partial \langle u_z \rangle_\psi / \partial r$ , is also listed for comparison. Due to the control input,  $\partial \langle u_r \rangle_\psi / \partial z$  drastically increases from negative to positive before the claw-like structure appears at  $\psi = 1.6\pi$ . Although the absolute value of  $\partial \langle u_r \rangle_\psi / \partial z$  is much smaller than  $\partial \langle u_z \rangle_\psi / \partial r$ , its relative strength also rises up to 7% at  $\psi = 1.6\pi$ . This positive  $\partial \langle u_r \rangle_\psi / \partial z$  works to suppress the negative production of  $PR_\theta^{\text{mix}}_\psi$ , because  $\partial \langle u_z \rangle_\psi / \partial r$  is always positive at the position of interest. Thus, the positive production of  $PR_r^{\text{mvg}}_\psi$  periodically stands out due to the periodic suppression of  $PR_\theta^{\text{mix}}_\psi$ .

## 6 Conclusions

DNS of controlled confined coaxial jet flow has been carried out. The following conclusions are derived on the control of near-field vortical structure and the consequent scalar transport processes.

Control using the intelligent nozzle is modelled by periodic contraction of the nozzle radius. The present control method generates various type of flow patterns and concentration profiles depending on the amplitude and the frequency of the contraction.

For the case of best mixing ( $St_a = 0.9$  and  $\varepsilon = 0.0125$ ), the mechanism of mixing enhancement can be explained as schematically shown in figure 25. First, a pair of counter-rotating two-dimensional vortex rings are synchronously discharged with the control input. Next, the scalar ejected from the central

nozzle is entrained by the inner vortex rings rolled up from the inner shear layer. The inner vortex rings that contain plenty of scalar are then distorted by the streamwise vortices near the centreline. Finally, the inner vortex rings become three-dimensional and break down, and this process enhances the mixing of scalar concentration.

The origin and the growth of the streamwise vortical structure are investigated by the phase-averaged transport equation of streamwise vorticity fluctuation. First, the present control makes seeds of streamwise vortices by attenuating the negative effect of azimuthal mixed production with positive  $\partial \langle u_r \rangle_\psi / \partial z$ . Next, the seeds of the streamwise vortices are stretched by  $\partial \langle u_z \rangle_\psi / \partial r$  of the coming roll-up vortices. Then, those vortices originated from the inner and outer shear layers start to develop in different manners. Development of the structure in the outer shear layer is essentially similar to that in ordinary mixing layers. The structure generated in the inner shear layer is convected toward the central axis and stretched axially by the periodically discharged inner vortex rings.

## Acknowledgments

The authors are grateful to Drs. Y. Suzuki and N. Shikazono (The University of Tokyo) for fruitful discussions and comments. This work was supported through the 21<sup>st</sup> Century COE Program, "Mechanical System Innovation", by the Ministry of Education, Culture, Sports, Science and Technology.

## References

- [1] Suzuki, H., Kasagi, N. and Suzuki, Y., 2004, Active control of an axisymmetric jet with distributed electromagnetic flap actuators. *Experiments in Fluids*, **36**, 498–509.
- [2] Kurimoto, N., Suzuki, Y. and Kasagi, N., 2005, Active control of lifted diffusion flames with arrayed micro actuators. *Experiments in Fluids*, **39**, 995–1008.
- [3] Kurimoto, N., 2005, *PhD Thesis The University of Tokyo*, in Japanese.
- [4] Angele, K., Kurimoto, N., Suzuki, Y. and Kasagi, N., 2005, The evolution of three-dimensional vortical structures in a coaxial jet controlled with micro flap-actuators. *Journal of Turbulence*, (submitted).
- [5] Danaïla, I., Dusek, J. and Anselmet, F., 1997, Direct numerical simulations of the free, unsteady, round, unforced jet at low Reynolds numbers. In Chollet, J.P., Voke, P.R. and Kleiser, L. (Eds), *Direct and Large-Eddy Simulation II*, pp. 1–10 (Dordrecht: Kluwer).
- [6] Boersma, B.J., Brethouwer, G. and Nieuwstadt, F.T.M., 1998, A numerical investigation on the effect of the inflow conditions on the self-similar region of a round jet. *Physics of Fluids*, **10**, 899–909.

- [7] da Silva, C.B., Balarac, G. and Métais, O., 2003, Transition in high velocity ratio coaxial jets analysed from direct numerical simulations. *Journal of Turbulence*, **4**(24).
- [8] Akselvoll, K. and Moin, P., 1996, Large-eddy simulation of turbulent confined coannular jets. *Journal of Fluid Mechanics*, **315**, 387–411.
- [9] Fukagata, K. and Kasagi, N., 2002, Highly energy-conservative finite difference method for the cylindrical coordinate system. *Journal of Computational Physics*, **181**, 478–498.
- [10] Harten, A., 1984, On a class of high resolution total-variation-stable finite difference schemes. *SIAM Journal on Numerical Analysis*, **21**, 1–23.
- [11] Sheen, H.J., Chen, W.J. and Wu, J.S., 1997, Flow patterns for an annular flow over an axisymmetric sudden expansion. *Journal of Fluid Mechanics*, **350**, 177–188.
- [12] Spalart, P.R., Moser, R.D. and Rogers, M.M., 1991, Spectral methods for the Navier-Stokes equations with one infinite and two periodic directions. *Journal of Computational Physics*, **96**, 297–324.
- [13] Dukowicz, J.K. and Dvinsky, A.S., 1992, Approximate factorization as a higher order splitting for the implicit incompressible flow equations. *Journal of Computational Physics*, **102**, 336–347.
- [14] Ethridge, F. and Greengard, L., 2001, A new fast-multipole accelerated Poisson solver in two dimensions. *SIAM Journal on Scientific Computing*, **23**, 741–760.
- [15] Mitsuishi, A., 2004, *Master Thesis The University of Tokyo*, in Japanese.
- [16] Hussain, A.K.M.F. and Zaman, K.B.M.Q., 1980, Vortex pairing in a circular jet under controlled excitation. Part 2. Coherent structure dynamics. *Journal of Fluid Mechanics*, **101**, 493–544.
- [17] Kurimoto, N., Suzuki, Y. and Kasagi, N., 2001, Active control of coaxial jet mixing and combustion with arrayed micro actuators. *Proceedings of the 5th World Conference on Experimental Heat Transfer, Fluid Mechanics and Thermodynamics*, pp. 511–516.
- [18] Pierrehumbert, R.T. and Widnall, S.E., 1982, The two- and three-dimensional instabilities of a spatially periodic shear layer. *Journal of Fluid Mechanics*, **114**, 59–82.
- [19] Lin, S.J. and Corcos, G.M., 1984, The mixing layer: deterministic models of a turbulent flow. Part 3. The effect of plane strain on the dynamics of streamwise vortices. *Journal of Fluid Mechanics*, **141**, 139–178.
- [20] Bernal, L.P. and Roshko, A., 1986, Streamwise vortex structure in plane mixing layers. *Journal of Fluid Mechanics*, **170**, 499–525.

- [21] Lasheras, J.C., Cho, J.S. and Maxworthy, T., 1986, On the origin and evolution of streamwise vortical structures in a plane, free shear layer. *Journal of Fluid Mechanics*, **172**, 231–258.
- [22] Liepmann, D. and Gharib, M., 1992, The role of streamwise vorticity in the near-field entrainment of round jets. *Journal of Fluid Mechanics*, **245**, 643–668.
- [23] Tennekes, H. and Lumley, J.L., 1972, *A First Course in Turbulence*, (Cambridge, MA: The MIT press).
- [24] Lasheras, J.C. and Choi, H., 1988, Three-dimensional instability of a plane free shear layer: an experimental study of the formation and evolution of streamwise vortices. *Journal of Fluid Mechanics*, **189**, 53–86.

Table 1: Mathematical expression and physical meaning of each term in the transport equation of the streamwise velocity fluctuation intensity.

|                               |   |  |
|-------------------------------|---|--|
| $CV_{r\psi}$                  | $-\langle u_r \rangle_\psi \frac{\partial}{\partial r} \langle \frac{1}{2} \omega_z'^2 \rangle_\psi$  | Radial convection by the phase-averaged velocity   |
| $CV_{z\psi}$                  | $-\langle u_z \rangle_\psi \frac{\partial}{\partial z} \langle \frac{1}{2} \omega_z'^2 \rangle_\psi$  | Axial convection by the phase-averaged velocity  |
| $TD_\psi$                     | $-\frac{\partial}{\partial r} \langle \frac{1}{2} u_r' \omega_z'^2 \rangle_\psi - \frac{\partial}{\partial z} \langle \frac{1}{2} u_z' \omega_z'^2 \rangle_\psi$  | Turbulent diffusion  |
| $VD_\psi$                     | $\frac{1}{\text{Re}} \left[ \frac{1}{r} \frac{\partial}{\partial r} \left( r \frac{\partial}{\partial r} \langle \frac{1}{2} \omega_z'^2 \rangle_\psi \right) + \frac{\partial^2}{\partial z^2} \langle \frac{1}{2} \omega_z'^2 \rangle_\psi \right]$ | Viscous diffusion  |
| $DS_\psi$                     | $-\frac{1}{\text{Re}} \left\langle \left( \frac{\partial \omega_z'}{\partial r} \right)^2 + \left( \frac{\partial \omega_z'}{r \partial \theta} \right)^2 + \left( \frac{\partial \omega_z'}{\partial z} \right)^2 \right\rangle_\psi$                | Viscous dissipation  |
| $PR_r^{\text{mvg}}_\psi$      | $\langle \omega_z' \omega_r' \rangle_\psi \frac{\partial \langle u_z \rangle_\psi}{\partial r}$   | Stretching of vorticity fluctuations by phase-averaged velocity gradient in radial direction |
| $PR_z^{\text{mvg}}_\psi$      | $\langle \omega_z'^2 \rangle_\psi \frac{\partial \langle u_z \rangle_\psi}{\partial z}$   | Stretching of vorticity fluctuations by phase-averaged velocity gradient in axial direction  |
| $PR_\theta^{\text{mix}}_\psi$ | $\langle \omega_\theta \rangle_\psi \left\langle \omega_z' \frac{\partial u_z'}{r \partial \theta} \right\rangle_\psi$  | Mixed production in azimuthal direction  |
| $PR_\psi^{\text{fv}}_\psi$    | $\left\langle \omega_z' \omega_r' \frac{\partial u_z'}{\partial r} + \omega_z' \omega_\theta' \frac{\partial u_z'}{r \partial \theta} + \omega_z'^2 \frac{\partial u_z'}{\partial z} \right\rangle_\psi$  | Stretching of vorticity fluctuations by fluctuating velocity gradient                        |

Table 2: Phase-averaged velocity gradient related to azimuthal mixed production right downstream of the inner nozzle edge.

| $\psi$  | $0\pi$  | $0.4\pi$ | $0.8\pi$ | $1.2\pi$ | $1.6\pi$ |
|---|---------|----------|----------|----------|----------|
| $\frac{\partial \langle u_r \rangle_\psi}{\partial z}$  | -0.0866 | -0.701   | -0.664   | 0.41     | 0.695    |
| $\frac{\partial \langle u_z \rangle_\psi}{\partial r}$  | 10.9    | 13.37    | 15.75    | 13.21    | 9.832    |
| $\frac{\partial \langle u_r \rangle_\psi}{\partial z} \bigg/ \frac{\partial \langle u_z \rangle_\psi}{\partial r} (\%)$ | -0.79   | -5.2     | -4.2     | 3.1      | 7.1      |

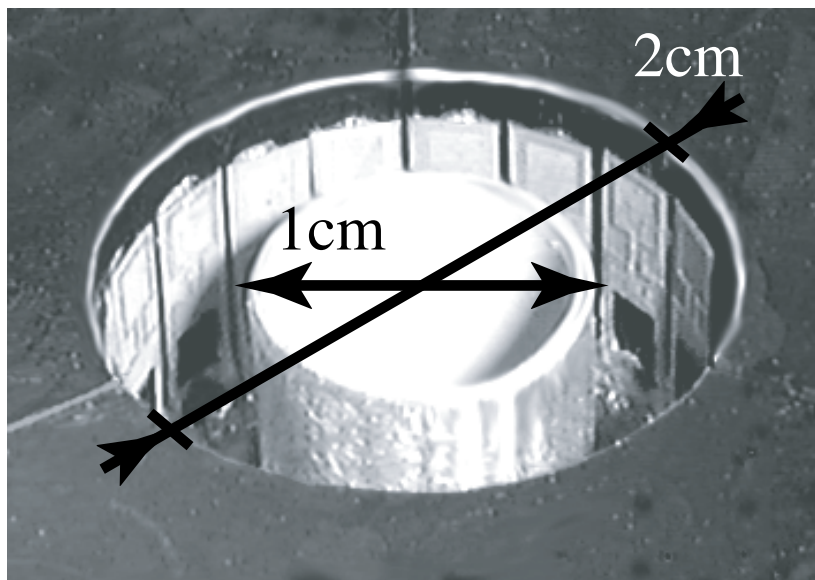


Figure 1: Intelligent nozzle [2].

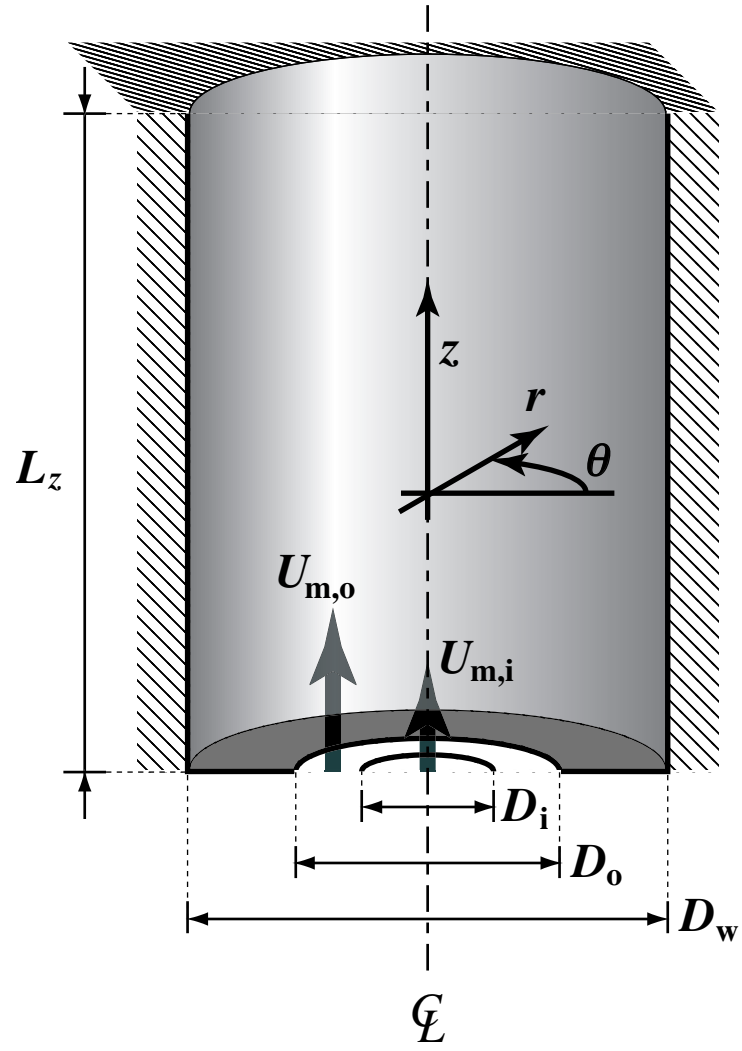


Figure 2: Computational model.

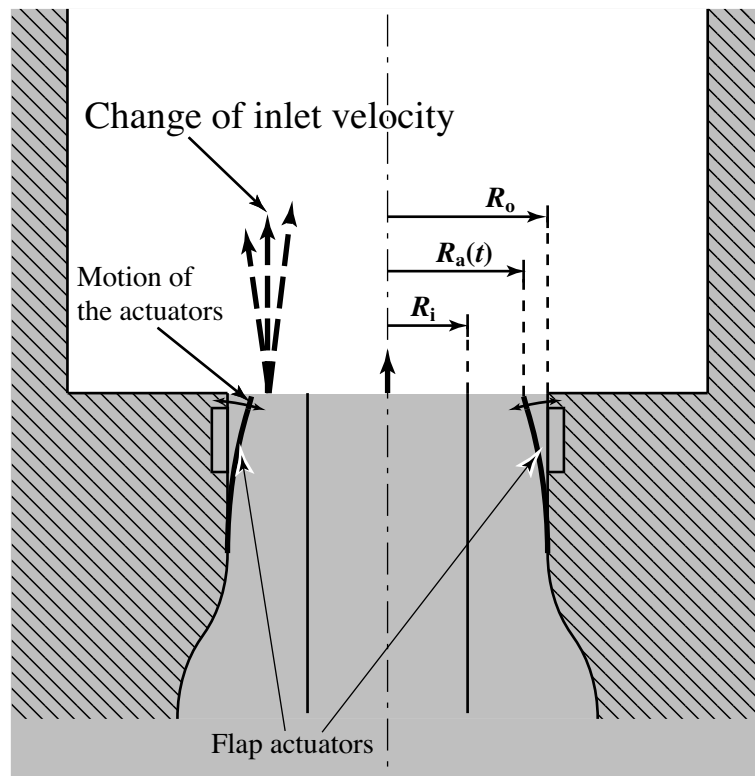


Figure 3: Schematic of actuators' motion.

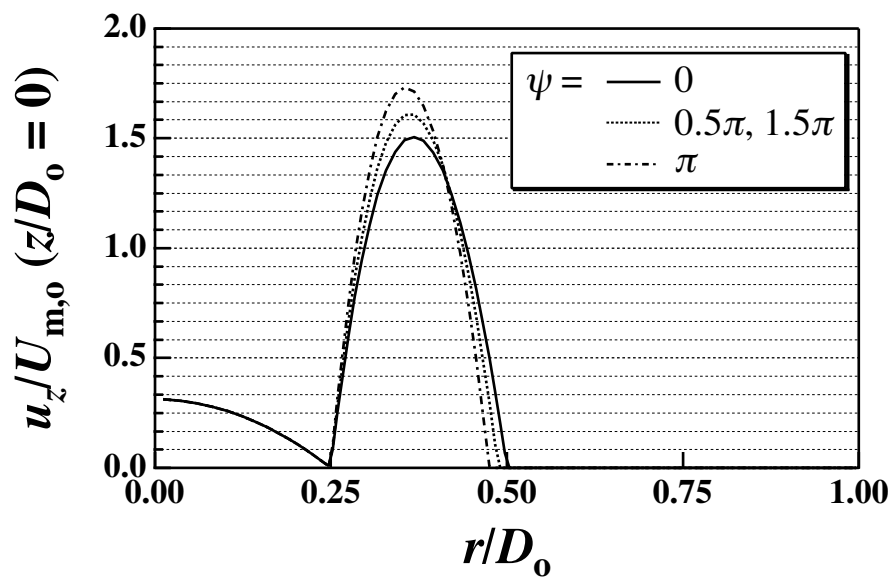


Figure 4: Inlet streamwise velocity profiles of different control phase angles.

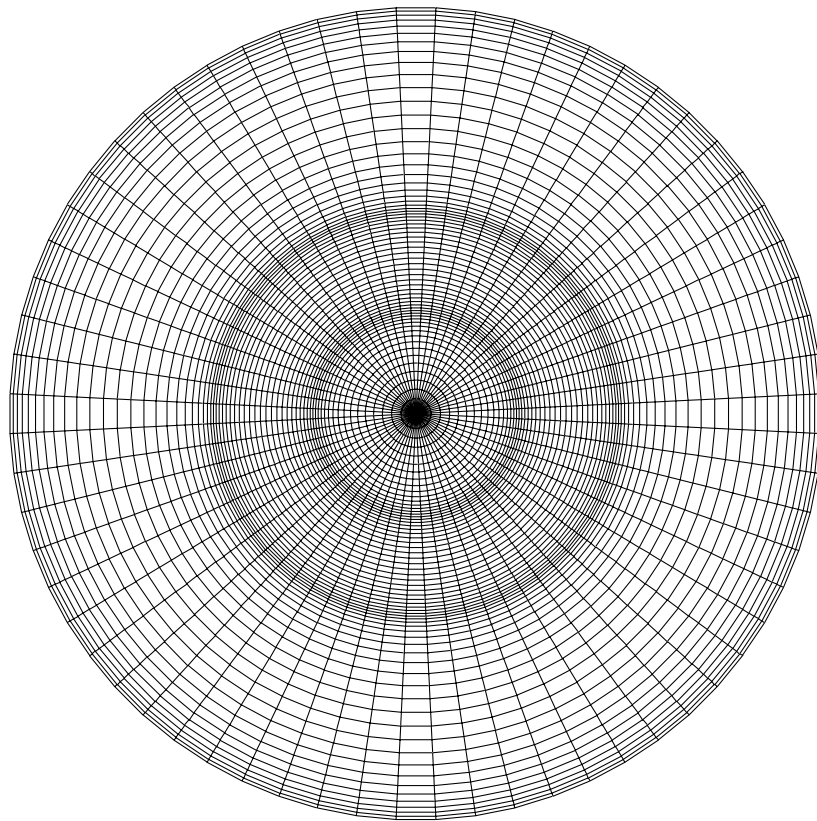


Figure 5: Computational grid in the cross-stream plane.

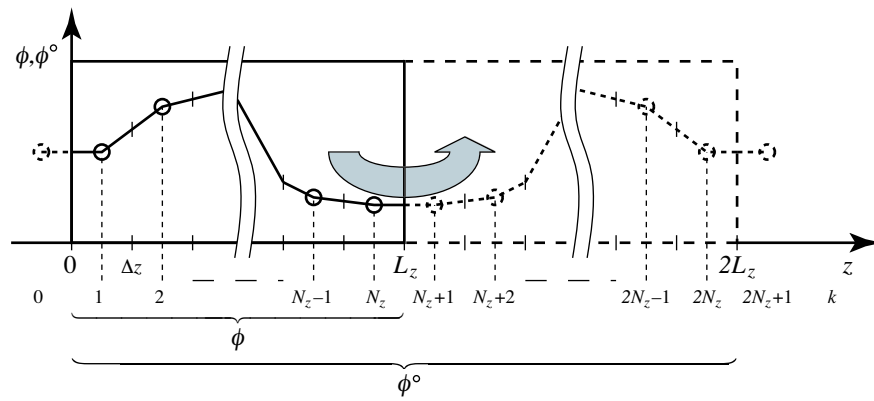


Figure 6: Schematic diagram of the even reflection operation.

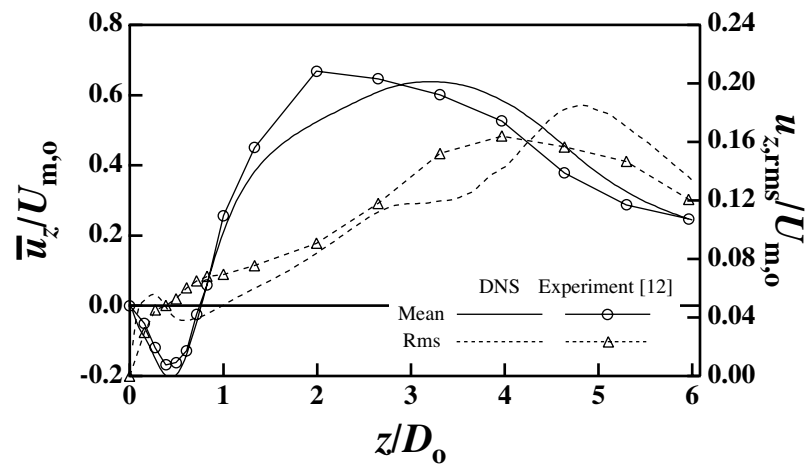


Figure 7: Mean and rms fluctuations of axial velocity along the central axis of an annular jet at  $Re = 1270$ .

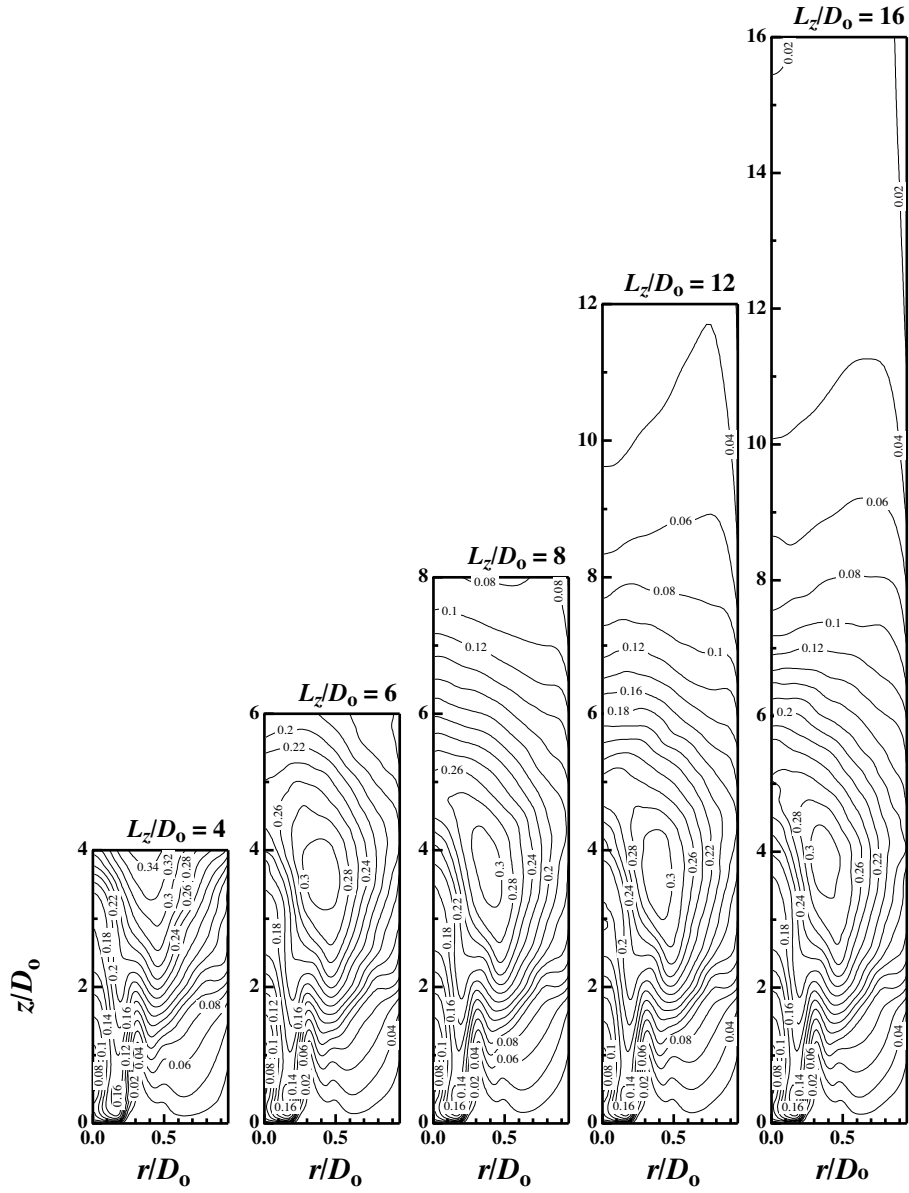


Figure 8: Rms fluctuations of streamwise velocity of an annular jet at  $Re = 1270$  with various domain lengths.

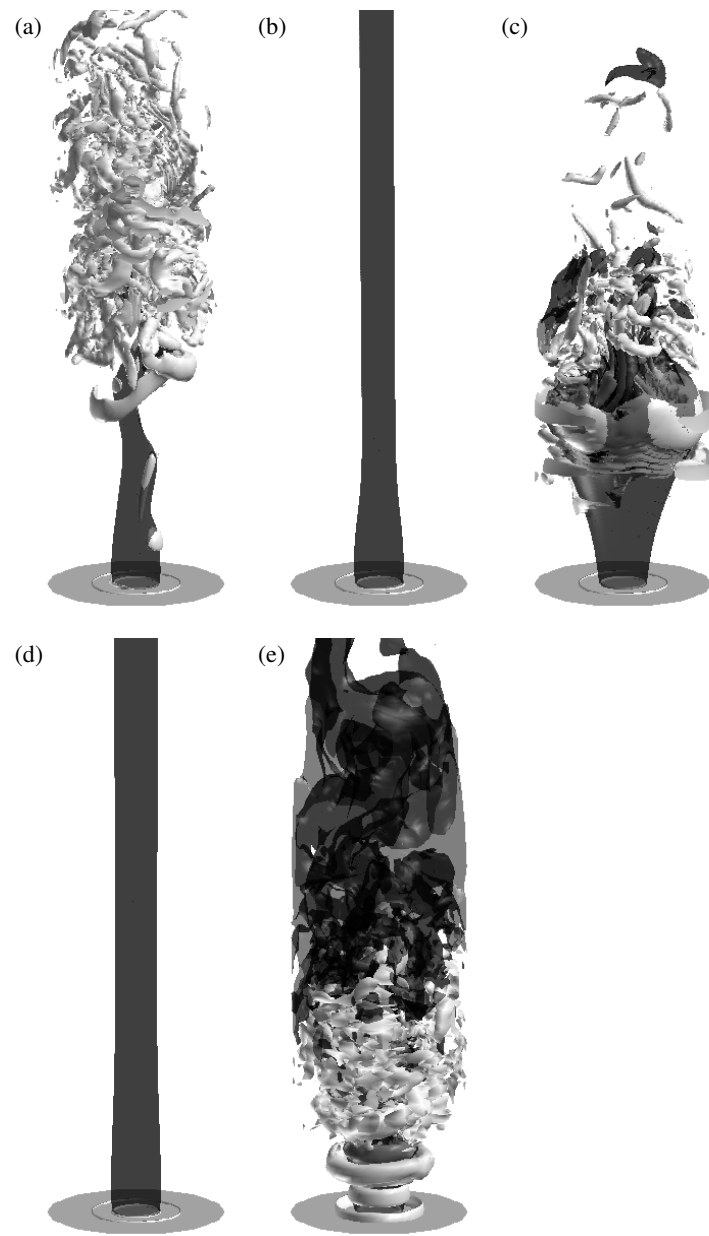


Figure 9: Instantaneous vortical structure (white) and scalar concentration distributions (black): natural jet with velocity ratio of (a)  $\beta = 32$ ; (b) 16; (c) 9.1; (d) 6.4; (e) controlled jet at  $St_a = 1$ ,  $\varepsilon = 0.0125$ .

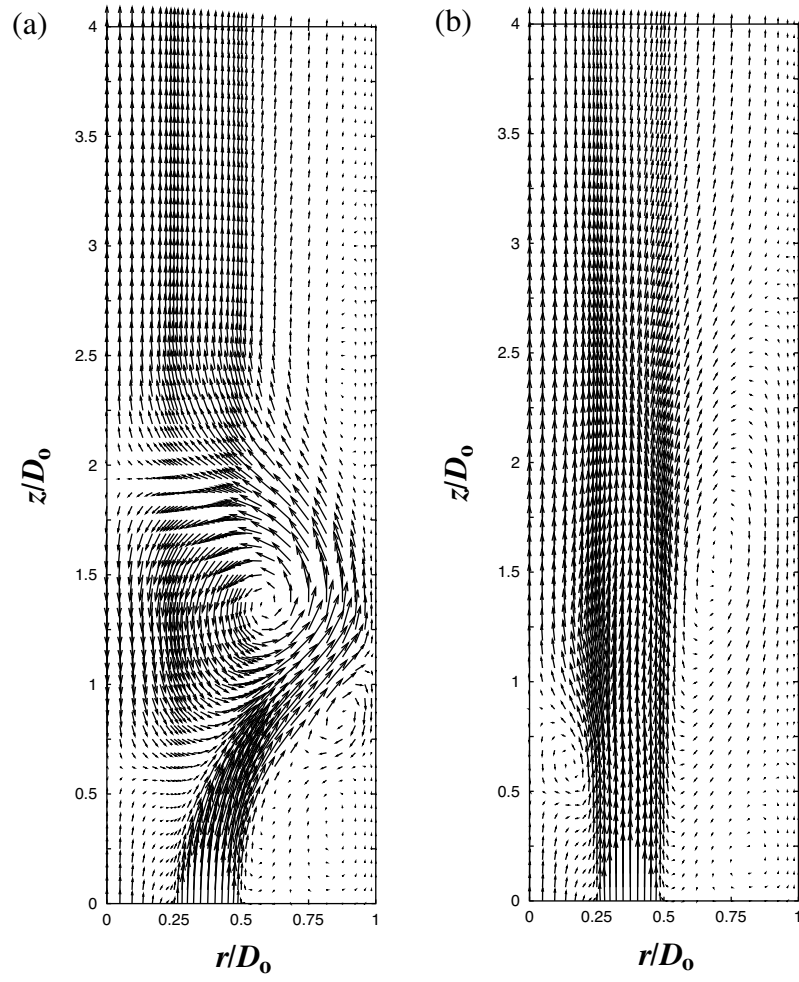


Figure 10: Mean velocity field for different control amplitudes: (a)  $\varepsilon = 0.001$ ; (b)  $\varepsilon = 0.01$ . Vectors are plotted every two grid points.

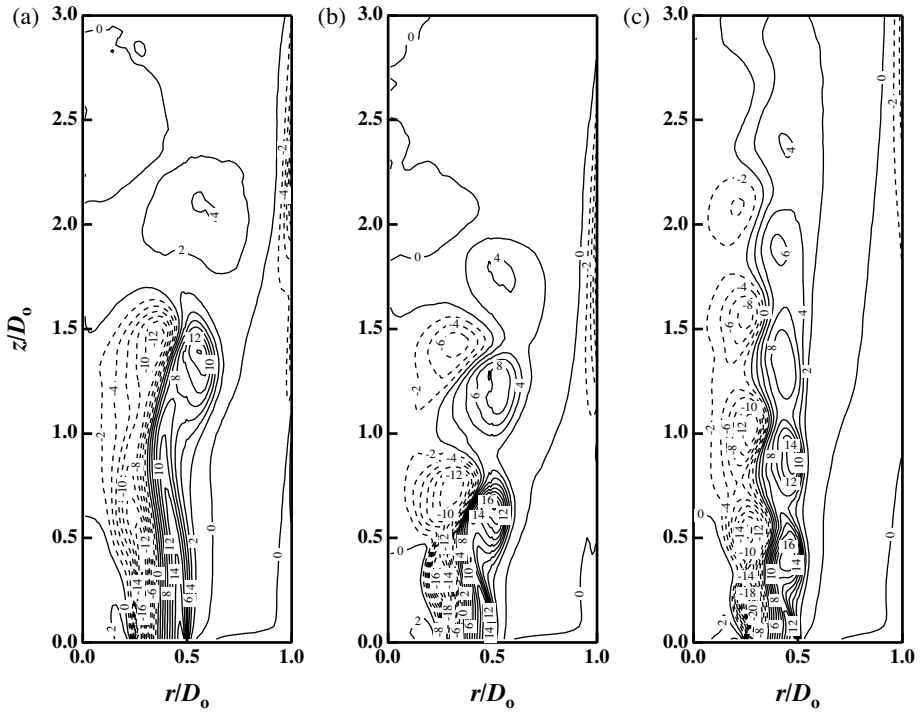


Figure 11: Phase-averaged azimuthal vorticity,  $\langle \omega_\theta \rangle_{1.6\pi}$ , at  $\varepsilon = 00125$ : (a)  $St_a = 0.5$ , (b)  $St_a = 1$ , (c)  $St_a = 1.5$ . Solid line,  $\langle \omega_\theta \rangle_{1.6\pi} \geq 0$ ; dashed line,  $\langle \omega_\theta \rangle_{1.6\pi} < 0$ .

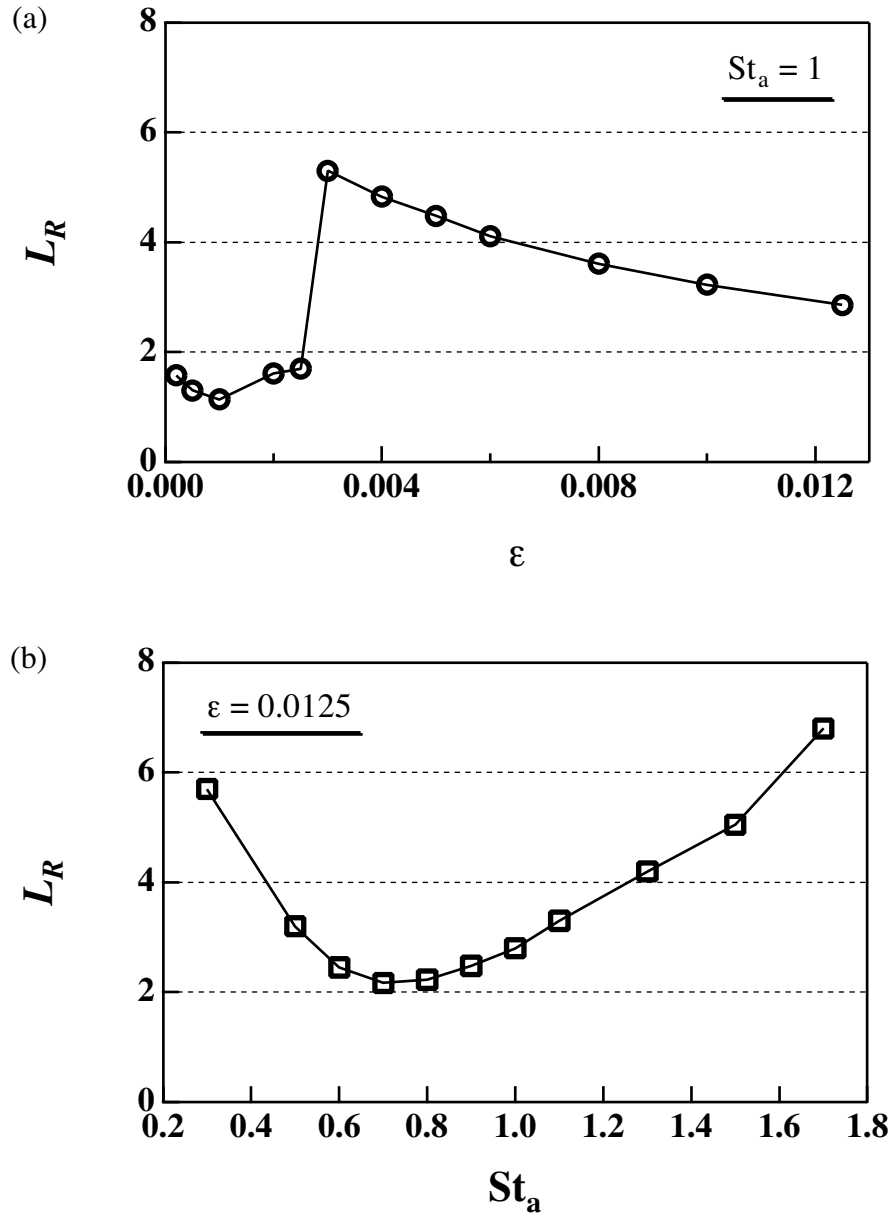


Figure 12: Relationship between the reattachment length and each control parameter: (a) control amplitude,  $\varepsilon$ ; (b) control frequency,  $St_a$ .

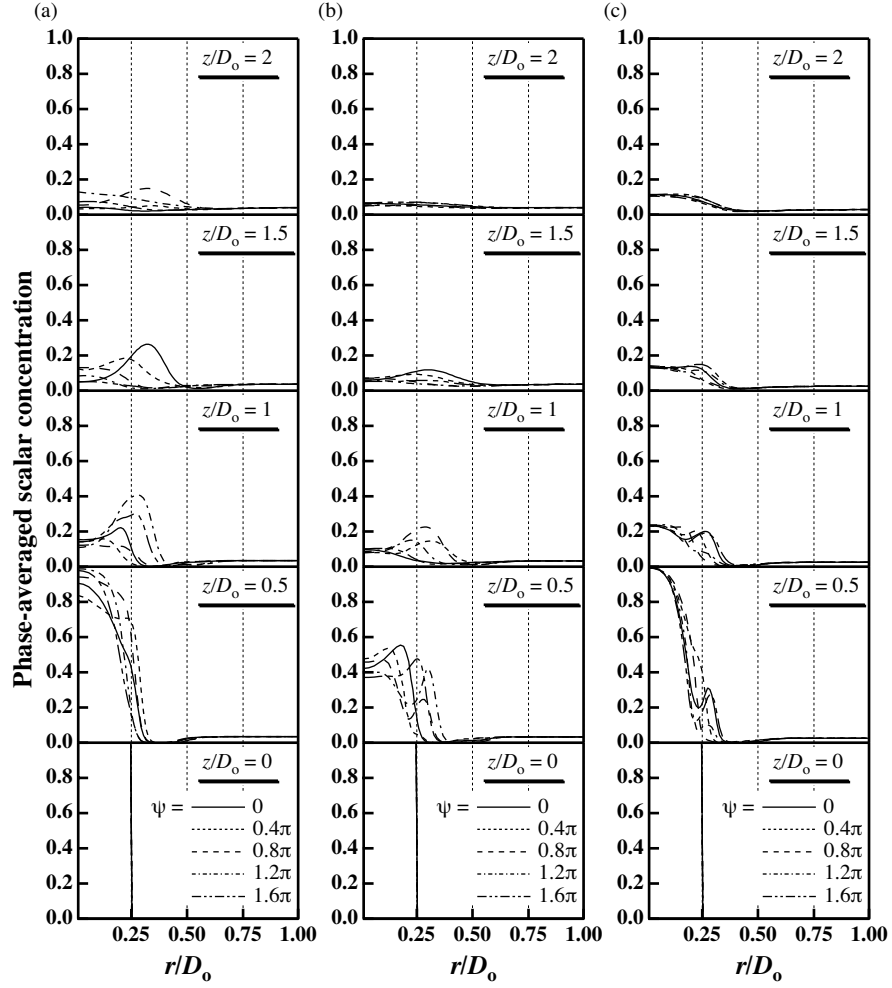


Figure 13: Effect of control frequency on the radial distributions of phase-averaged scalar concentration at  $\varepsilon = 0.0125$ : (a)  $St_a = 0.5$ ; (b)  $St_a = 1$ ; (c)  $St_a = 1.5$ .

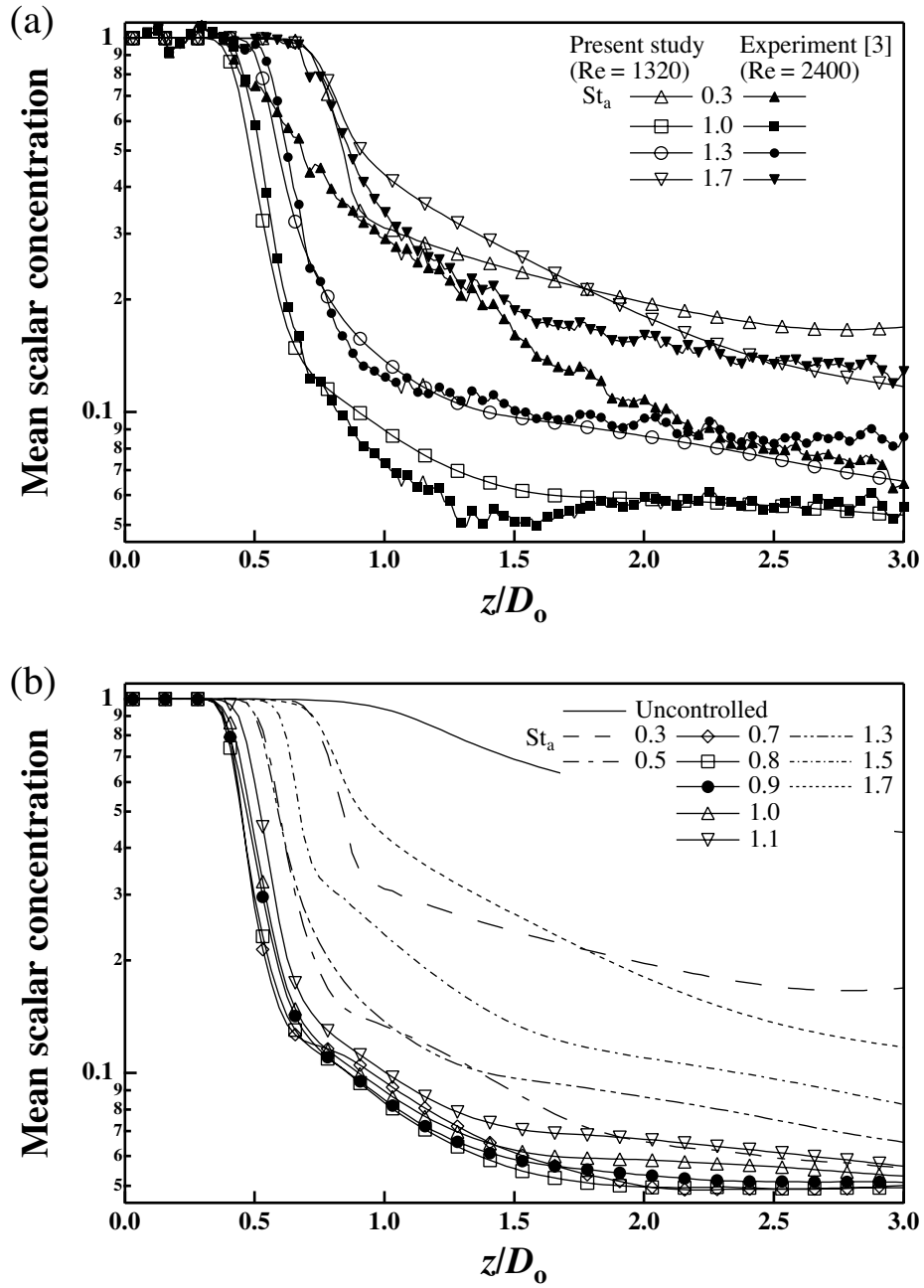


Figure 14: The mean scalar concentration along the central axis at  $\varepsilon = 0.0125$ : (a) comparison with previous experiment [3]; (b) the effect of control frequency.

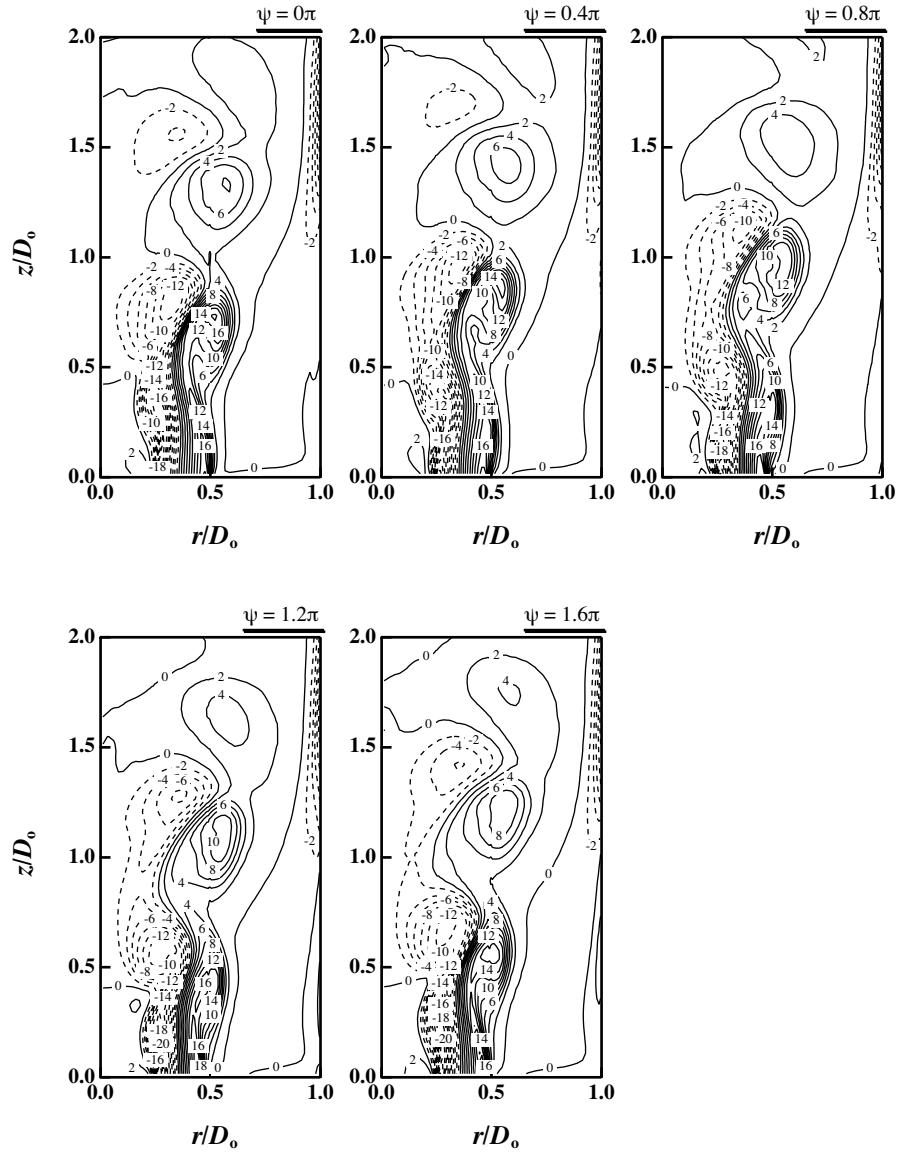


Figure 15: Phase-averaged azimuthal vorticity,  $\langle \omega_\theta \rangle_\psi$ , at  $\varepsilon = 0.0125$ ,  $St_a = 0.9$ . Solid line,  $\langle \omega_\theta \rangle_\psi \geq 0$ ; dashed line,  $\langle \omega_\theta \rangle_\psi < 0$ .

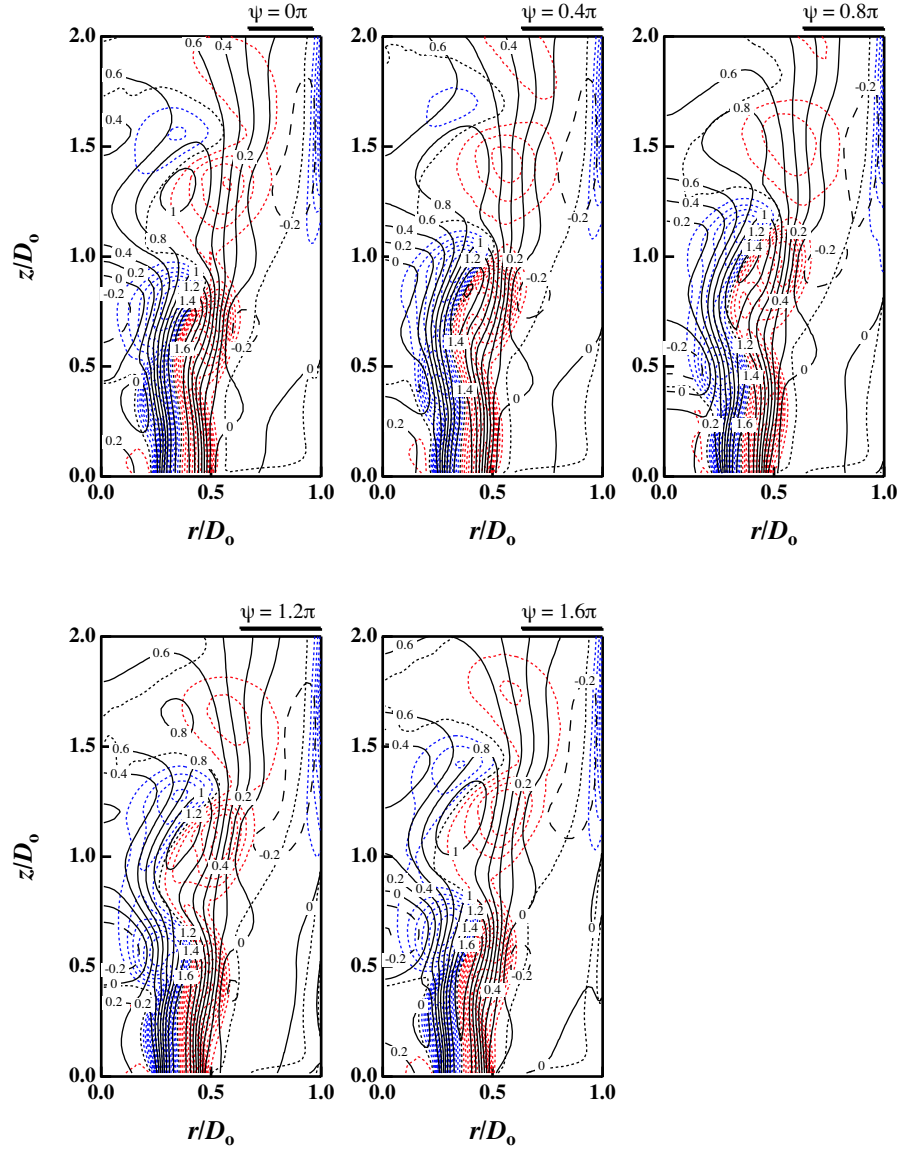


Figure 16: Spatial relationship between phase-averaged axial velocity,  $\langle u_z \rangle_\psi$ , (solid line,  $\langle u_z \rangle_\psi \geq 0$ ; dashed line,  $\langle u_z \rangle_\psi < 0$ ), and azimuthal vorticity (dotted line: red,  $\langle \omega_\theta \rangle_\psi > 0$ ; black,  $\langle \omega_\theta \rangle_\psi = 0$ ; blue,  $\langle \omega_\theta \rangle_\psi < 0$ ) at  $\varepsilon = 0.0125$ ,  $St_a = 0.9$ .

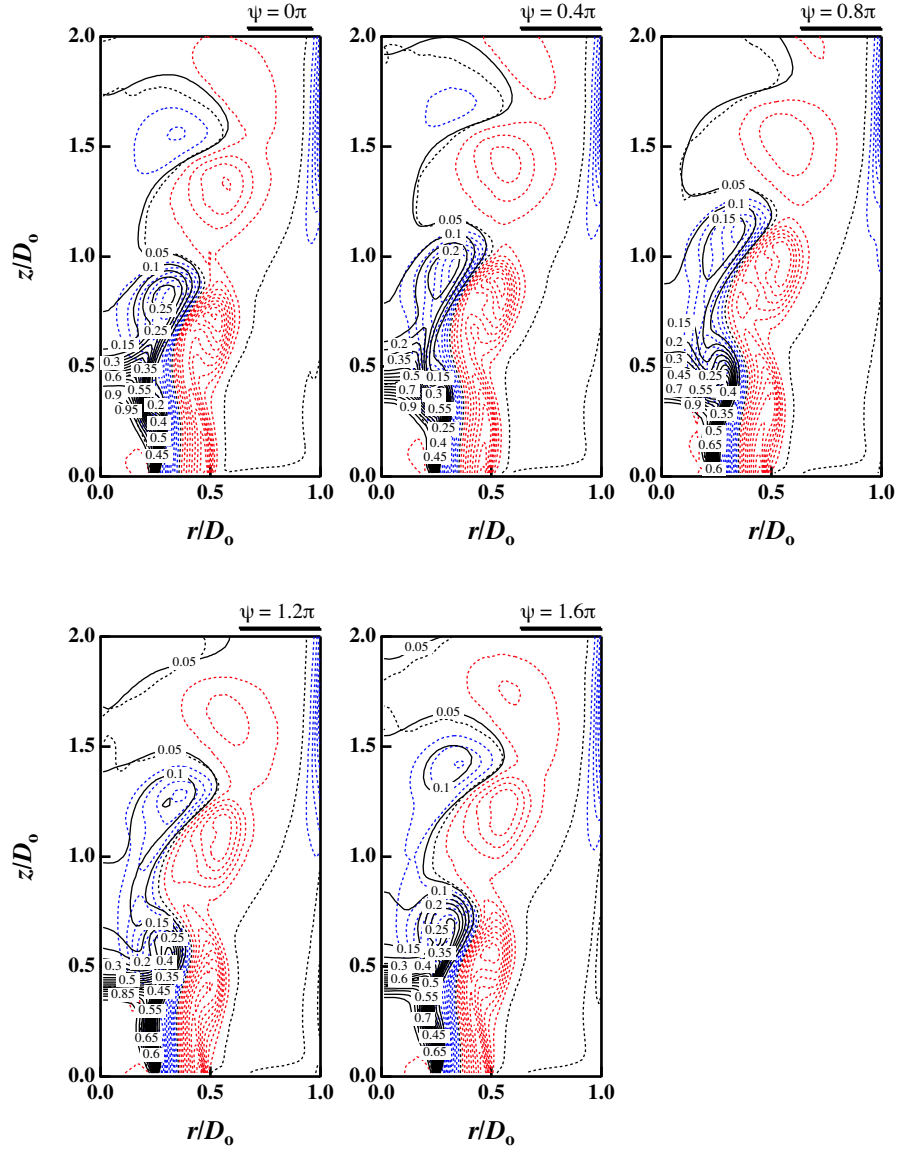


Figure 17: Spatial relationship between phase-averaged scalar concentration,  $\langle c \rangle_{\psi}$ , (solid line), and azimuthal vorticity (dotted line: red,  $\langle \omega_{\theta} \rangle_{\psi} > 0$ ; black,  $\langle \omega_{\theta} \rangle_{\psi} = 0$ ; blue,  $\langle \omega_{\theta} \rangle_{\psi} < 0$ ) at  $\varepsilon = 0.0125$ ,  $St_a = 0.9$ .

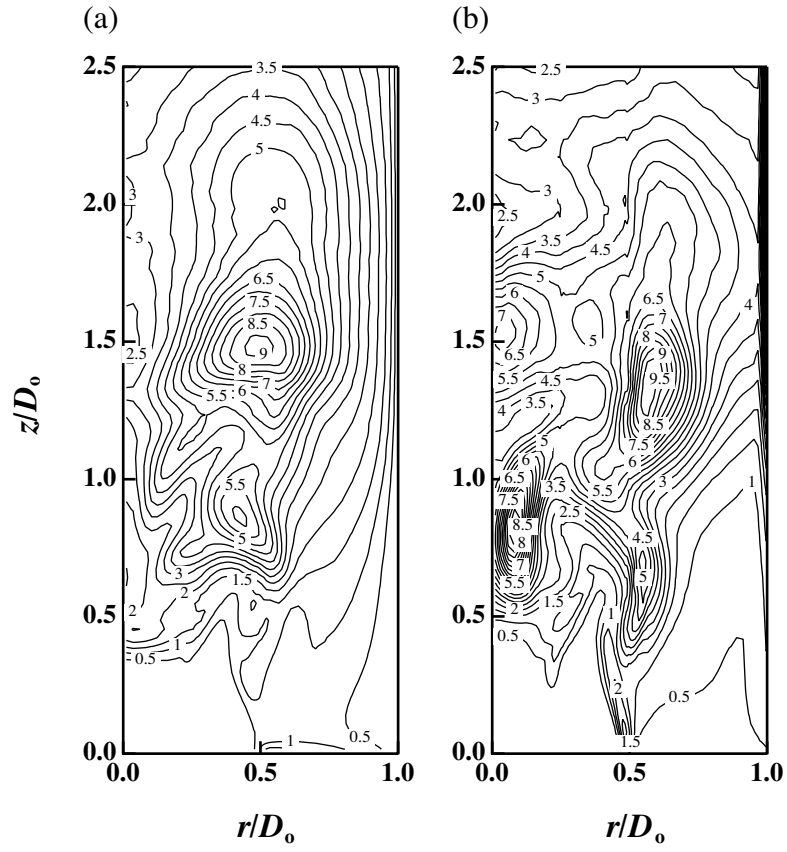


Figure 18: Phase-averaged vorticity fluctuation at  $\varepsilon = 0.0125$ ,  $St_a = 0.9$ ,  $\psi = 1.6\pi$ . (a)  $\langle \omega_{r,rms} \rangle_\psi$ , (b)  $\langle \omega_{z,rms} \rangle_\psi$ .

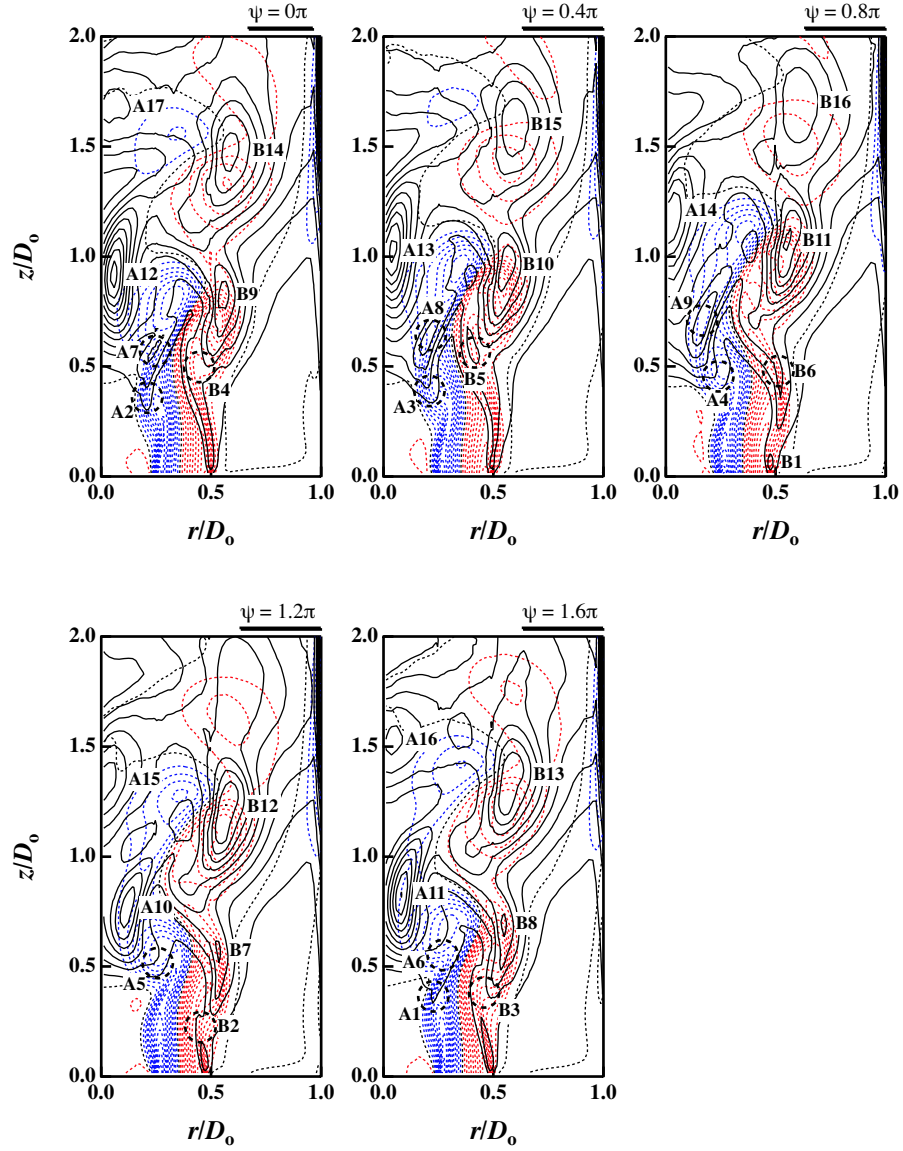


Figure 19: Phase-averaged axial vorticity fluctuation,  $\langle \omega_z \rangle_{\psi, \text{rms}}$ , (solid line), and azimuthal vorticity (dotted line: red,  $\langle \omega_\theta \rangle_{\psi} > 0$ ; black,  $\langle \omega_\theta \rangle_{\psi} = 0$ ; blue,  $\langle \omega_\theta \rangle_{\psi} < 0$ ) at  $\varepsilon = 0.0125$ ,  $\text{St}_a = 0.9$ .

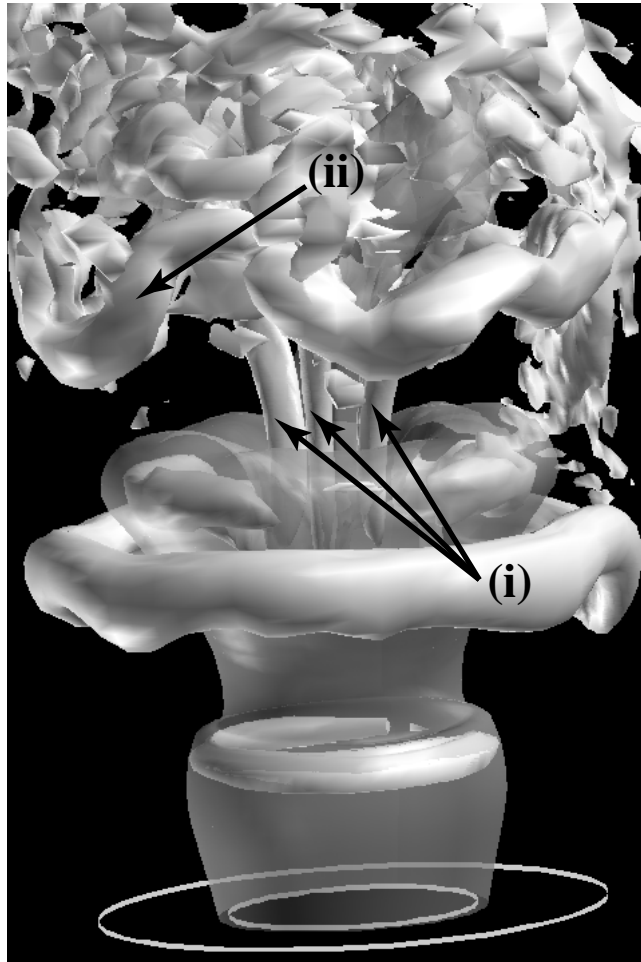


Figure 20: Instantaneous vortical structure (white opaque) and scalar isosurface (gray transparent).

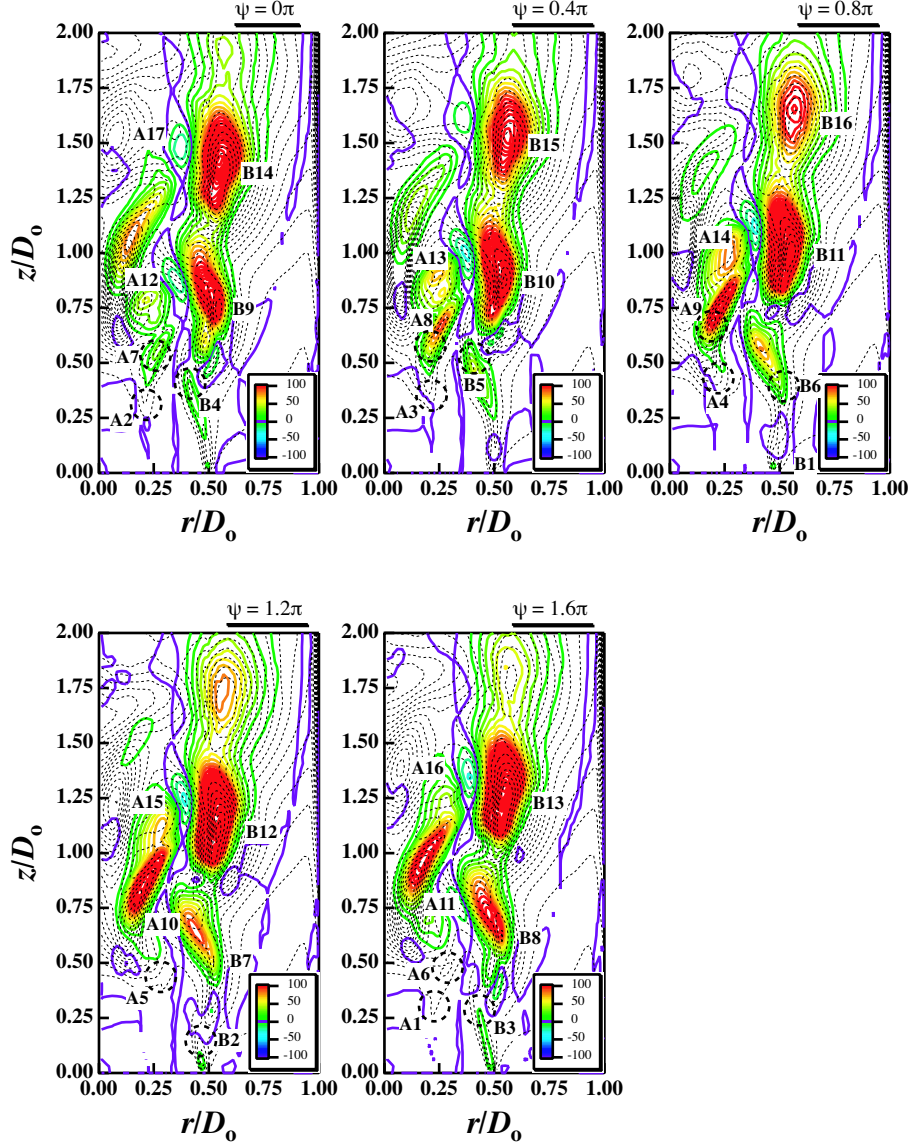


Figure 21: Spatial relationship between phase-averaged radial stretching,  $PR_r^{\text{mvg}}_\psi$  (coloured line; purple line represents  $PR_r^{\text{mvg}}_\psi = 0$ ), and streamwise vorticity fluctuation,  $\langle \omega_z \rangle_{\psi, \text{rms}}$  (dotted line) at  $\varepsilon = 0.0125$ ,  $St_a = 1$ .

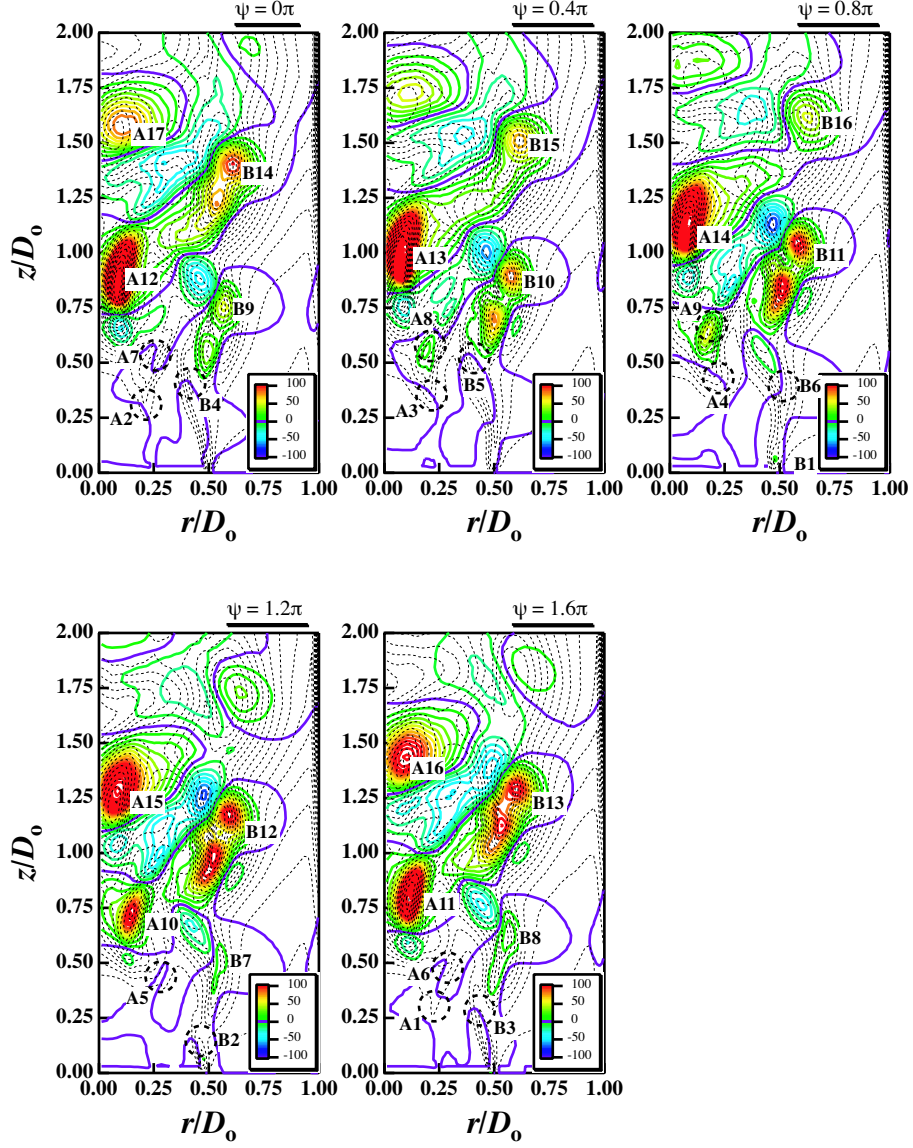


Figure 22: Spatial relationship between phase-averaged axial stretching,  $PR_z^{\text{mvg}_\psi}$  (coloured line; purple line represents  $PR_z^{\text{mvg}_\psi} = 0$ ), and streamwise vorticity fluctuation,  $\langle \omega_z \rangle_{\psi, \text{rms}}$  (dotted line) at  $\varepsilon = 0.0125$ ,  $St_a = 1$ .

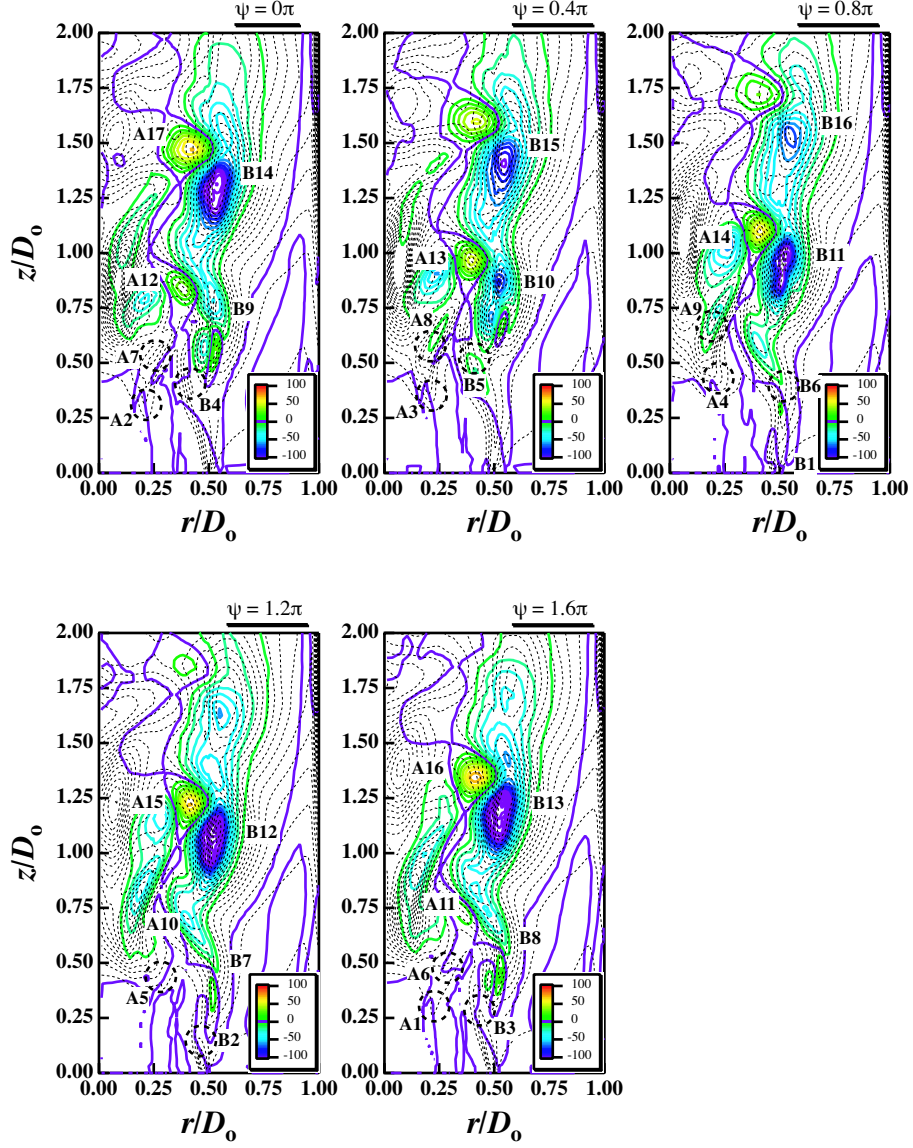


Figure 23: Spatial relationship between phase-averaged azimuthal mixed production,  $PR_{\theta}^{\text{mix}}_{\psi}$  (coloured line; purple line represents  $PR_{\theta}^{\text{mix}}_{\psi} = 0$ ), and stream-wise vorticity fluctuation,  $\langle \omega_z \rangle_{\psi, \text{rms}}$  (dotted line) at  $\varepsilon = 0.0125$ ,  $St_a = 1$ .

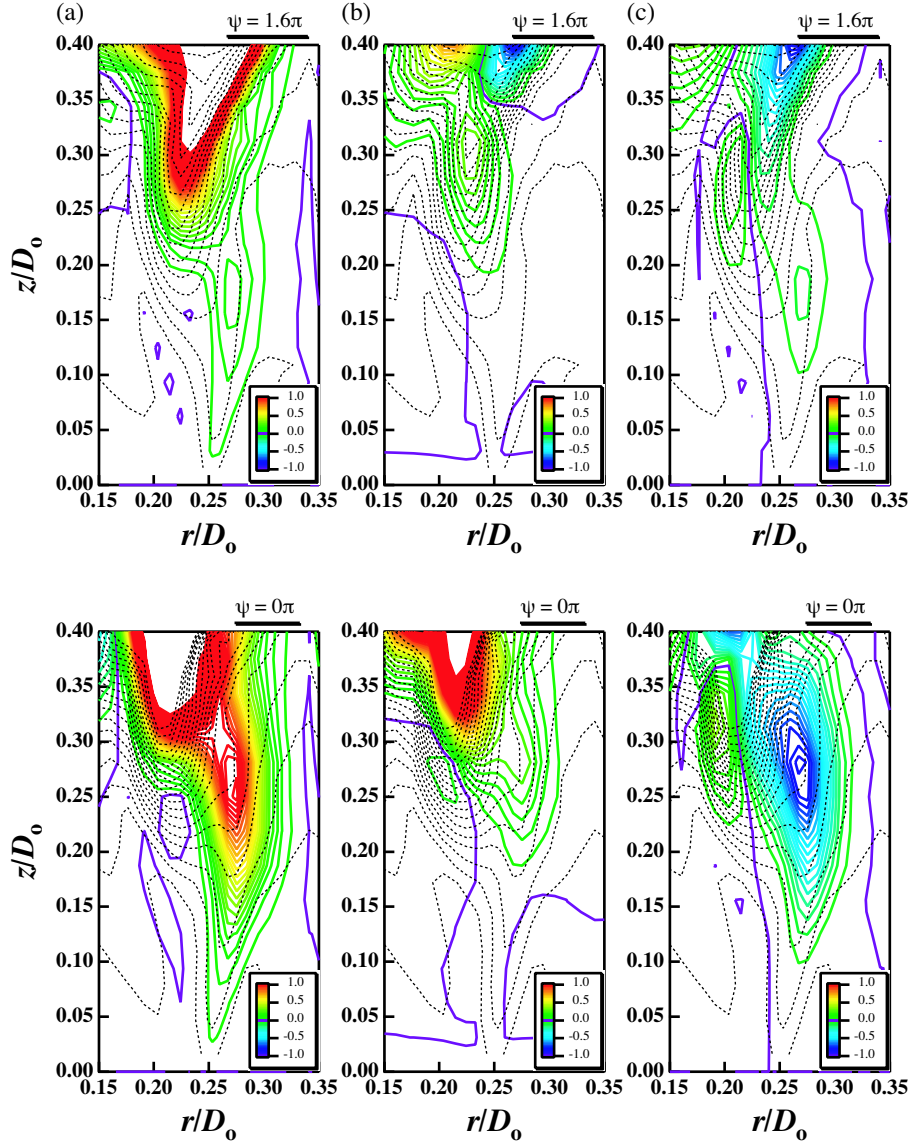


Figure 24: Closeup pictures of (a)  $PR_r^{\text{mvg}}_{\psi}$ , (b)  $PR_z^{\text{mvg}}_{\psi}$ , (c)  $PR_{\theta}^{\text{mix}}_{\psi}$  at the near-nozzle inner shear layer, together with  $\langle \omega_z \rangle_{\psi, \text{rms}}$ , at  $\varepsilon = 0.0125$ ,  $St_a = 1$  ( $\psi = 1.6\pi$  and  $\psi = 0\pi(2\pi)$ ). Coloured line with purple line as zero, each production term; dotted line,  $\langle \omega_z \rangle_{\psi, \text{rms}}$ .

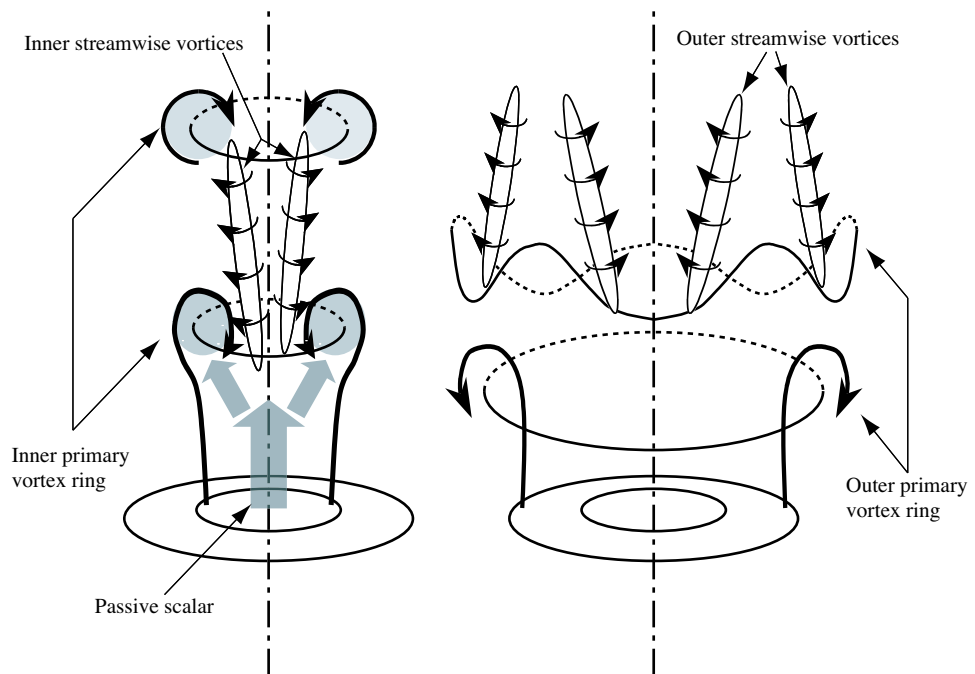


Figure 25: Schematic diagram of scalar transport processes due to near-field large-scale vortical structure of (a) the inner and (b) the outer shear layers.